2006-06

Autonomous time-frequency cropping and feature-extraction algorithms for classification of LPI radar modulations

Zilberman, Eric R.

Monterey, California. Naval Postgraduate School

NAVAL POSTGRADUATE SCHOOL

MONTEREY, CALIFORNIA

THESIS

AUTONOMOUS TIME-FREQUENCY CROPPING AND FEATURE-EXTRACTION ALGORITHMS FOR CLASSIFICATION OF LPI RADAR MODULATIONS

by

Eric R. Zilberman

June 2006

Thesis Advisor: Phillip E. Pace

Approved for public release; distribution is unlimited.

THIS PAGE INTENTIONALLY LEFT BLANK

REPORT DOCUMENTATION PAGE			Form Approved OMB No. 0704-0188
Public reporting burden for this collection of information is estimated to average 1 hour per response, including the time for reviewing instruction, searching existing data sources, gathering and maintaining the data needed, and completing and reviewing the collection of information. Send comments regarding this burden estimate or any other aspect of this collection of information, including suggestions for reducing this burden, to Washington headquarters Services, Directorate for Information Operations and Reports, 1215 Jefferson Davis Highway, Suite 1204, Arlington, VA 22202-4302, and to the Office of Management and Budget, Paperwork Reduction Project (0704-0188) Washington DC 20503.			
1. AGENCY USE ONLY ***(Leave blank)***	**2. REPORT DATE** June 2006	**3. REPORT TYPE AND DATES COVERED** Master's Thesis	
4. TITLE AND SUBTITLE: Autonomous Time-Frequency Cropping and Feature-Extraction Algorithms for Classification of LPI Radar Modulations			**5. FUNDING NUMBERS**
6. AUTHOR Eric R. Zilberman			
7. PERFORMING ORGANIZATION NAME(S) AND ADDRESS(ES) Naval Postgraduate School Center for Joint Services Electronic Warfare Monterey, CA 93943-5000			**8. PERFORMING ORGANIZATION REPORT NUMBER**
9. SPONSORING /MONITORING AGENCY NAME(S) AND ADDRESS(ES) Office of Naval Research Code 313 Arlington, VA 22209			**10. SPONSORING/MONITORING AGENCY REPORT NUMBER**
11. SUPPLEMENTARY NOTES The views expressed in this thesis are those of the author and do not reflect the official policy or position of the Department of Defense or the U.S. Government.			
12a. DISTRIBUTION / AVAILABILITY STATEMENT Approved for public release; distribution is unlimited.			**12b. DISTRIBUTION CODE** A

13. ABSTRACT

Three autonomous cropping and feature extraction algorithms are examined that can be used for classification of low probability of intercept radar modulations using time-frequency (T-F) images. The first approach, Erosion Dilation Adaptive Binarization (EDAB), uses erosion and a new adaptive threshold binarization algorithm embedded within a recursive dilation process to determine the modulation energy centroid (radar's carrier frequency) and properly place a fixed-width cropping window. The second approach, Marginal Frequency Adaptive Binarization (MFAB), uses the marginal frequency distribution and the adaptive threshold binarization algorithm to determine the start and stop frequencies of the modulation energy to locate and adapt the size of the cropping window. The third approach, Fast Image Filtering, uses the fast Fourier transform and a Gaussian low-pass filter to isolate the modulation energy. The modulation is then cropped from the original T-F image and the adaptive binarization algorithm is used again to compute a binary feature vector for input into a classification network. The binary feature vector allows the image detail to be preserved without overwhelming the classification network that follows. A multi-layer perceptron and a radial basis function network are used for classification and the results are compared. Classification results for nine simulated radar modulations are shown to demonstrate the three feature-extraction approaches and quantify the performance of the algorithms. It is shown that the best results are obtained using the Choi-Williams distribution followed by the MFAB algorithm and a multi-layer perceptron. This setup produced an overall percent correct classification (Pcc) of 87.2% for testing with noise variation and 77.8% for testing with modulation variation. In an operational context, the ability to process and classify LPI signals autonomously allows the operator in the field to receive real-time results.

14. SUBJECT TERMS Choi-Williams, Wiger-Ville, BPSK, time-frequency, autonomous, LPI, feature extraction, multi-layer perceptron, radial basis function			**15. NUMBER OF PAGES** 94
			16. PRICE CODE
17. SECURITY CLASSIFICATION OF REPORT Unclassified	**18. SECURITY CLASSIFICATION OF THIS PAGE** Unclassified	**19. SECURITY CLASSIFICATION OF ABSTRACT** Unclassified	**20. LIMITATION OF ABSTRACT** UL

NSN 7540-01-280-5500 Standard Form 298 (Rev. 2-89)
Prescribed by ANSI Std. 239-18

THIS PAGE INTENTIONALLY LEFT BLANK

Approved for public release; distribution is unlimited.

AUTONOMOUS TIME-FREQUENCY CROPPING AND FEATURE-EXTRACTION ALGORITHMS FOR CLASSIFICATION OF LPI RADAR MODULATIONS

Eric R. Zilberman
Ensign, United States Navy
B.S., United States Naval Academy, 2005

Submitted in partial fulfillment of the
requirements for the degree of

MASTER OF SCIENCE IN SYSTEMS TECHNOLOGY

from the

NAVAL POSTGRADUATE SCHOOL
June 2006

Author: Eric R. Zilberman

Approved by: Phillip E. Pace
Thesis Advisor

Don Brutzman
Second Reader

Dan Boger
Chair, Department of Information Sciences

THIS PAGE INTENTIONALLY LEFT BLANK

ABSTRACT

Three autonomous cropping and feature extraction algorithms are examined that can be used for classification of low probability of intercept radar modulations using time-frequency (T-F) images. The first approach, Erosion Dilation Adaptive Binarization (EDAB), uses erosion and a new adaptive threshold binarization algorithm embedded within a recursive dilation process to determine the modulation energy centroid (radar's carrier frequency) and properly place a fixed-width cropping window. The second approach, Marginal Frequency Adaptive Binarization (MFAB), uses the marginal frequency distribution and the adaptive threshold binarization algorithm to determine the start and stop frequencies of the modulation energy to locate and adapt the size of the cropping window. The third approach, Fast Image Filtering, uses the fast Fourier transform and a Gaussian low-pass filter to isolate the modulation energy. The modulation is then cropped from the original T-F image and the adaptive binarization algorithm is used again to compute a binary feature vector for input into a classification network. The binary feature vector allows the image detail to be preserved without overwhelming the classification network that follows. A multi-layer perceptron and a radial basis function network are used for classification and the results are compared. Classification results for nine simulated radar modulations are shown to demonstrate the three feature-extraction approaches and quantify the performance of the algorithms. It is shown that the best results are obtained using the Choi-Williams distribution followed by the MFAB algorithm and a multi-layer perceptron. This setup produced an overall percent correct classification (Pcc) of 87.2% for testing with noise variation and 77.8% for testing with modulation variation. In an operational context, the ability to process and classify LPI signals autonomously allows the operator in the field to receive real-time results.

THIS PAGE INTENTIONALLY LEFT BLANK

TABLE OF CONTENTS

LIST OF FIGURES

LIST OF TABLES

THIS PAGE INTENTIONALLY LEFT BLANK

ACKNOWLEDGMENTS

Thank you to Professor Phillip Pace for keeping my research focused on the task at hand during my short stay at NPS. Thank you to my family and friends for their support. The research and learning required to complete this thesis was rewarding and will be of great use as I continue my Naval career.

This work was supported by the Office of Naval Research, ONR code 313, Arlington, VA. A special thanks goes to Dr. Peter Craig and Mr. Mike Monsma for their continuing support and encouragement.

THIS PAGE INTENTIONALLY LEFT BLANK

I. INTRODUCTION

A. AUTONOMOUS CLASSIFICATION OF LPI RADAR

The low probability of intercept (LPI) radar has established itself as the premier tactical radar in the civilian and military spectrum. Table 1 gives examples of current LPI radars, their use, and their manufacturer. Applications include radar altimeters, surveillance, navigation, aviation automatic landing systems, target acquisition radars, tracking radars, and many more systems that require LPI characteristics.

Table 1. Current LPI Radar Systems Under Production [1]

Developer	System	LPI Use
NavCom Defense Electronics	AN/APN-232	Combined altitude radar altimeter
Honeywell	HG-9550	Radar altimeter
NAVAIR	GRA-2000	Tri-service radar altimeter
Tellumat, South Africa	PA-5429	Radar altimeter
Thompson CSF	AHV-2100	Radar altimeter
BAE	AD1990	Radar altimeter
Textron Systems	TALS	Precision approach, automatic landing
Sierra Nevada	TALS	Tactical automatic landing system
Saab Bofors	Pilot	Surveillance, navigation
Signaal	Scout	Surveillance, navigation
Signaal	Smart-L	Surveillance
Ericsson Microwave Systems	HARD-3D	Fire control and surveillance
Ericsson Microwave Systems	Eagle	Fire control
Ericsson Microwave Systems	Pointer	Air surveillance radar
Pitt Research Institute, Poland	CRM-100	Surface target detection
China Inst. Of Elec. Engineering	JY-17A	Battlefield surveillance radar
Raytheon	MRSR	Target acquisition and tracking radar
T1	AN/APS-147	Enhanced search and target designation
Raytheon	AN/APQ-181	Tactical multimode fire control radar
Northrop Grumman	AN/APG-77	Multimode tactical radar
Raytheon	AN/APG-70	Multimode tactical radar
T1	LANTIRN	Terrain following radar
Saab Dynamics	RPS-15MR	Radar guided air-to-surface missile
BAE	Spearfish	Torpedo for littoral environments

The term LPI is that property of radar that, because of its lower power, wide bandwidth, frequency variability, or other design attributes, make it difficult for it to be detected by means of a passive intercept receiver [1]. Radars with such capabilities help eliminate many of the security vulnerabilities normally associated with radar transmission; with LPI radar, a user can transmit a signal confidently knowing the probability is low that the transmitted signal will not be intercepted by a passive intercept receiver.

The common attributes that characterize LPI radars are [2]:

- Low average power continuous wave (CW) radiation with a large time-bandwidth product.
- Radiated energy spread over a wide angular region, long time interval, and wide frequency band.
- Ultra-low side lobe transmit antenna.
- Power management is employed to radiate only when necessary to measure target characteristics and at a level that is consistent with the radar cross section of the targets to be detected.
- Atmospheric attenuation shielding is sometimes used at high frequencies to limit reception by an intercept receiver (short range emitter).

The mathematical characteristic that allows for minimal detection by a passive intercept receiver is defined by the ratio of the range at which an intercept receiver on board a platform can detect the LPI radar to the range at which the platform can be detected by the LPI radar [3]. To directly compare the radar detection range and the intercept receiver detection range the ratio, α, of the two maximum detection ranges is given as [1]

$$\alpha = \frac{R_{\mathrm{Im}ax}}{R_{R\max}} \tag{1.1}$$

where $R_{\mathrm{Im}ax}$ is the maximum intercept receiver passive emission detection range and $R_{R\max}$ is the maximum radar receiver target detection range. The variable α is a

performance parameter that has been proposed to quantify the quality of a LPI radar by determining the likelihood of a LPI radar being detected. If $\alpha > 1$ the radar may be detected by an intercept receiver at a range greater than the radar can detect targets. If $\alpha = 1$ the radar can detect targets at the same range that the intercept receiver can detect the radar emissions, and if $\alpha < 1$ the radar can detect targets at a further range than the intercept receiver can detect the radar's emissions. [1, 3, 4].

There are two hats to wear when analyzing LPI radars. The first hat is that of the offensive emitter operator that needs to minimize traces of his presence for mission completion. The other hat involves defensive tactics and the ability to detect and classify the presence of the offensive operator's emissions in order to conduct counter operations. This thesis examines new autonomous detection, feature extraction, and classification techniques in order to help the defensive operator counter the threat of the offensive LPI operator. These techniques reduce the human operator burden to detect and classify these types of LPI emitters.

B. PRINCIPAL CONTRIBUTION

Autonomously classifying LPI Radar CW modulations is a four-step process. Figure 1 illustrates the four signal processing steps that take place at the intercept receiver. First, using a mathematical formula a signal is generated that models the sampled LPI radar modulations. The signal is detected using a time-frequency distribution. The time-frequency image is then processed in order to extract a feature vector containing the modulation. After the feature vector is extracted, a neural network is used to identify the LPI radar CW modulation.

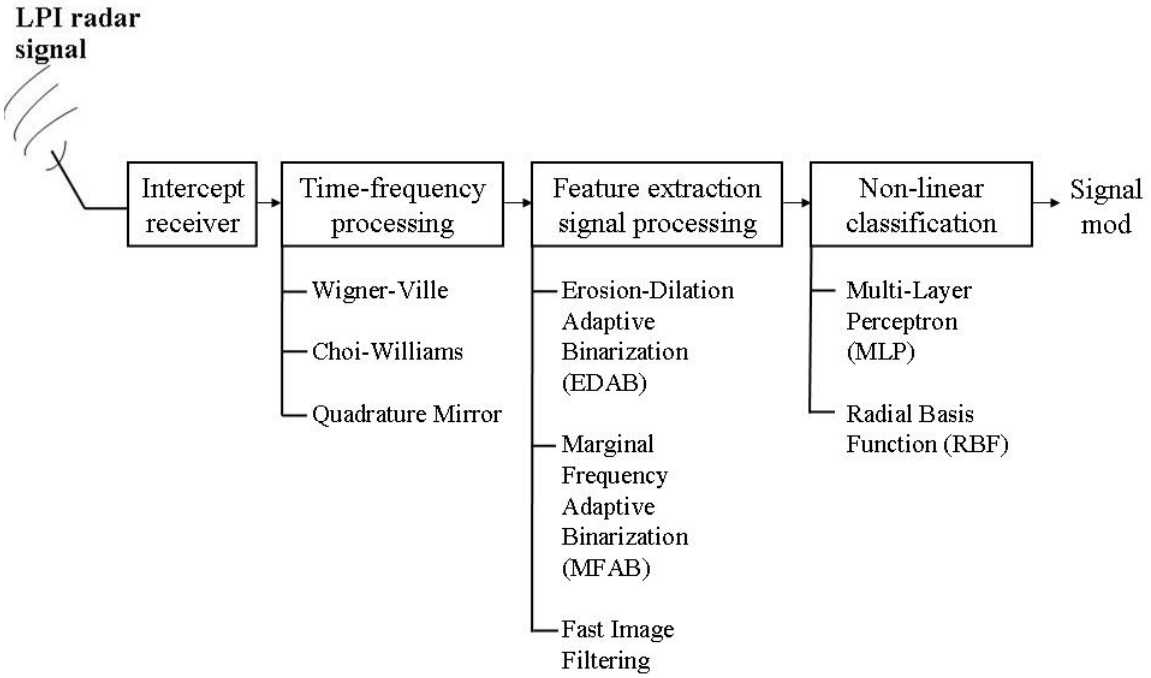

Figure 1. Block Diagram of Intercept Receiver Signal Processing.

Prior to this thesis, the software responsible for processing the images of LPI signals was programmed to know that all of the generated signals were coming in on a carrier frequency of 1 kHz (f_c = 1 kHz). Realistically, signals are not always generated at 1 kHz. To simulate an environment that emulates real-world scenarios, it was necessary to generate a database that consisted of signals that were similar to what one might find in an operational environment. Three databases are investigated in this thesis. The first database consists of LPI signal modulations at a single carrier frequency of 1 kHz. A second, more diverse database, was generated that contained signals at two different carrier frequencies. A database with multiple carrier frequencies is more synonymous to an actual operational environment. The third database is the most diverse of the three. It contained signals at two different carrier frequencies with multiple SNRs. Not only does this database better mimic the operational environment, but it also tests the autonomous feature extraction algorithms discussed in this thesis.

Three time-frequency processing techniques are investigated. The Wigner-Ville distribution, the Choi-Williams distribution, and the Quadrature Mirror Filter Bank approach are examined and the advantages and disadvantages of each are discussed and compared.

Three autonomous cropping and feature extraction algorithms were investigated to extract the modulation energy from the T-F images. The first algorithm, Erosion Dilation Adaptive Binarization (EDAB), uses morphological operations along with a new adaptive binarization process. The second algorithm, Marginal Frequency Adaptive Binarization (MFAB), uses a marginal frequency distribution along with the adaptive binarization process and the third algorithm, Fast Image Filtering, uses the fast Fourier transform and a Gaussian low pass filter to crop the modulation energy.

Neural Networks are the closest way to simulate how the human brain processes information. A neural network is able to learn its own algorithm for the classification task with actual samples of data [5]. Neural networks are often used to classify sets of data; unknown information comes into the neural network, and the neural network is able to identify and classify the information. It is able to do this by training on known sets of data and then comparing new sets of data to the known sets to correctly classify the data. There are many ways to implement a neural network. The multi-layer perceptron (MLP) and the radial-basis function (RBF) are both investigated to test their applicability to classify a LPI signal using the feature vector from the time-frequency detection images.

C. THESIS OUTLINE

This thesis is organized as follows:

Chapter II briefly describes the LPI radar signals that are used to exercise the feature extraction and classification networks. Specifically Frequency Modulated Continuous Wave signals (FMCW), polyphase coded signals such as the Frank, P1, P2, P3, and P4, and poly-time code signals such as T1(n) and T2(n) (n is the number of phase states) are investigated. Also investigated are Binary Phase Shift Keying (BPSK) signals; although not LPI, they provide a good benchmark since they are also used in communication systems which are now appearing in the radar spectrum.

Chapter III presents the time-frequency distributions used for detection. The Wigner-Ville distribution, Choi-Williams distribution, and Quadrature Mirror Filter Bank approach are described.

Chapter IV describes the three autonomous cropping and feature extraction algorithms used to isolate the modulation energy from the LPI signals. The autonomous

feature extraction algorithm uses morphological operations to extract the modulation energy from the LPI signal and is called the Erosion-Dilation Adaptive Binarization (EDAB) technique. A Marginal Frequency Adaptive Binarization (MFAB) algorithm is presented and the investigation of a 2-D Fast Fourier Transform (FFT) technique for filtering is described.

Chapter V describes the three different databases that consist of the many LPI signals used to test the different feature extraction algorithms.

Chapter VI investigates the two different classifiers used to classify the LPI signals. A multi-layer perceptron (MLP) network and a radial-basis function (RBF) network are both examined.

Chapter VII presents the classification results and discusses the advantages and disadvantages of the different algorithms.

Chapter VIII concludes the thesis and recommends future work.

II. LOW PROBABILITY OF INTERCEPT (LPI) SIGNAL MODULATIONS

In this chapter nine LPI radar modulations are described: FMCW, Frank, P1, P2, P3, P4, T1(*n*), T2(*n*). Although not a LPI signal the BPSK modulation is also described. These nine modulations are used to test the feature extraction algorithms presented in Chapter IV.

A. FREQUENCY MODULATION CONTINUOUS WAVE (FMCW)

Frequency Modulation Continuous Wave (FMCW) emitters are often associated with LPI because of their ability to measure a target's range and rate without transmitting a lot of power [6]. Detection of the target's range and range rate are done by varying the transmit frequency in the time domain and then measuring the frequency of the return signal [1]. FMCW emitters are a popular approach to maintain stealthy LPI characteristics and robustness against electronic attack because of the following:

- The frequency modulation spreads the transmitted energy over a large modulation bandwidth ΔF .
- Interception of the emitter's signal is difficult because the power spectrum of the FMCW signal is nearly rectangular over the modulation bandwidth.
- The transmit waveform is deterministic and the transmit power is low.
- FMCW modulations are compatible with solid-state transmitters (power management).
- FMCW is easier to implement than phase code modulation.

The FMCW waveform consists of two linear frequency modulation sections with both positive and negative slopes [6]. The transmit signal for the first section is given by [1, 7]

$$s_1(t) = a_0 \sin 2\pi\left(\left(f_c - \frac{\Delta F}{2}\right)t + \frac{\Delta F}{2t_m}t^2\right) \tag{2.1}$$

where f_c is the RF carrier, ΔF is the transmit modulation bandwidth, and t_m is the modulation period with $0 < t < t_m$. The transmit baseband signal for the second section is given by [1, 7]

$$s_2(t) = a_0 \sin 2\pi \left[\left(f_c + \frac{\Delta F}{2} \right) t - \frac{\Delta F}{2t_m} t^2 \right] \tag{2.2}$$

for $t_m < t < 2t_m$. A triangular FMCW signal is shown in Figure 2. Note that the bandwidth is denoted as ΔF, the carrier frequency is denoted as f_c, and the modulation period is denoted as t_m.

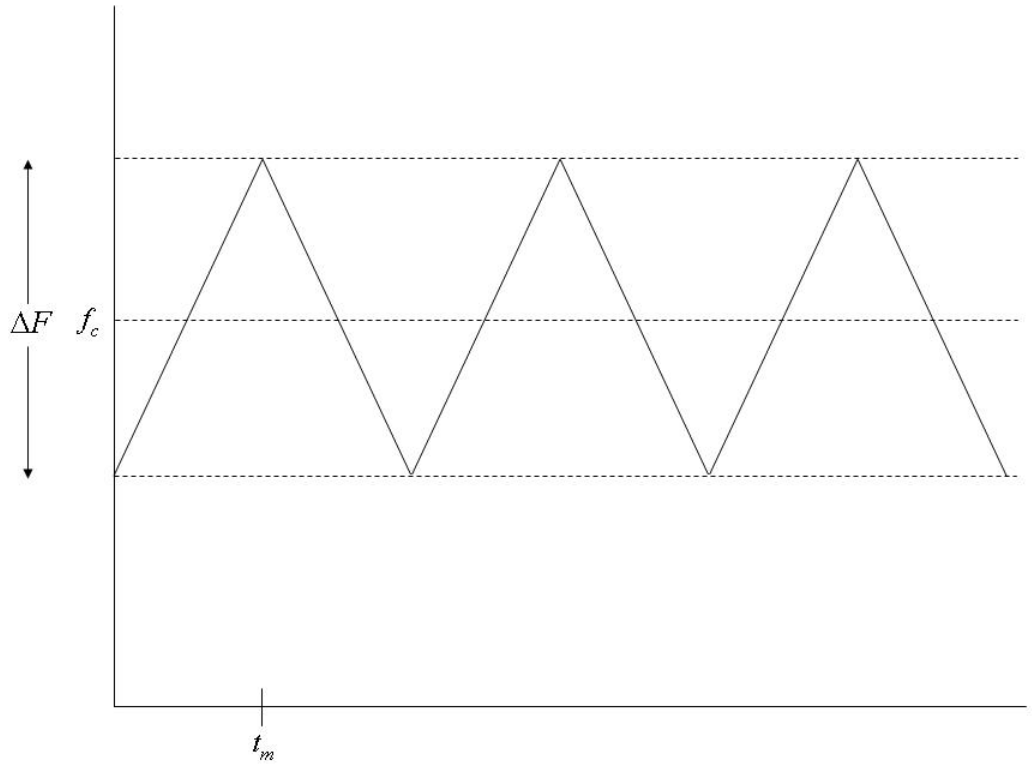

Figure 2. Triangular FMCW LPI Signal.

B. POLYPHASE CODE FRANK

In 1963, R.L. Frank devised a polyphase code that is closely related to the linear frequency modulation and Barker codes [1, 6, 8]. Barker codes can not be used successfully in LPI emitters because they can easily be detected by a frequency doubling

circuit. They also have high energy time side lobes. Frank codes are characterized by having a perfect autocorrelation function and minimum side lobes [8].

The Frank code is derived from a step approximation to a linear frequency modulation waveform using *M* frequency steps and *M* samples per frequency. A code length or processing gain (number of phase sub-codes) is given as [6]

$$N_c = M^2 \tag{2.3}$$

The phase of the *i*th sample of the *j*th frequency is

$$\phi_k = \phi_{i,j} = \frac{2\pi}{M}(i-1)(j-1) \tag{2.4}$$

where *i* is the number of the sample in a given frequency (*i* = 1, 2, ..., *M*) and *j* is the frequency steps (*j* = 1, 2, …, *M*) [6]. The peak side lobe level is given as

$$PSL = 20\log_{10}\left(\frac{1}{M\pi}\right) \tag{2.5}$$

The phase shift in radians and the unwrapped signal phase shift in radians versus the sub-code index for phase change for a Frank signal with M = 8, N_c = 64, f_c = 1 kHz, f_s (sampling frequency) = 7 kHz, and *cpp* (carrier cycles per subcode) = 1 is shown in Figure 3. Note that the code change is largest at the center of the code (indicated by black arrow). From (2.5) the *PSL* of this signal is -28 dB.

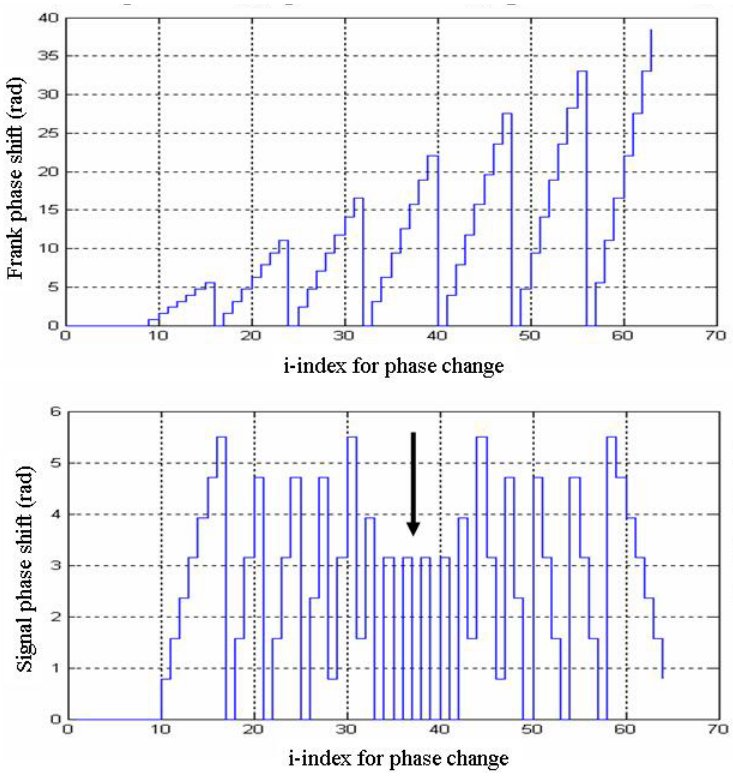

Figure 3. Frank Phase Shift and Unwrapped Phase Shift (radians) vs. Index for Phase Change.

C. POLYPHASE CODE P1

The polyphase codes are derived from a linear-frequency-modulation waveform and a step-approximation to a linear frequency modulation waveform [1, 9]. The P1 signal and the rest of the polyphase compression codes (P1, P2, P3, P4) have many useful features such as low time side lobes and the possibility of a large number of sub-codes. A reduction in the size of side lobes makes all of the polyphase compression codes useful in scenarios where LPI is needed.

The P1 code is derived by altering the Frank code. The Frank code groups have the largest phase changes from code element to code element in the center of the uncompressed pulse. The P1 code is designed to be more Doppler tolerant than the Frank code by having the largest phase changes occur at the ends of the code [10]. The P1 code is given by

$$\phi_{i,j} = \frac{-\pi}{M}[M-(2j-1)][(j-1)M+(i-1)] \tag{2.6}$$

where i is the number of the sample in a given frequency (i = 1, 2, …, M), j is the number of the frequency (j = 1, 2, …, M) resulting in M frequency steps and M samples per frequency. The processing gain, N_c, is the number of phase codes

$$N_c = M^2 \tag{2.7}$$

where M = 1, 2, 3… [1, 9]. The peak side lobe level is also given by

$$PSL = 20\log_{10}(1/M\pi) \tag{2.8}$$

The phase shift and unwrapped phase shift for a P1 signal with M = 8, N_c = 64, f_c = 1 kHz, f_s = 7 kHz, and cpp = 1 is shown in Figure 4. The code change is largest for the P1 signal at the ends of the code (indicated by black arrows).

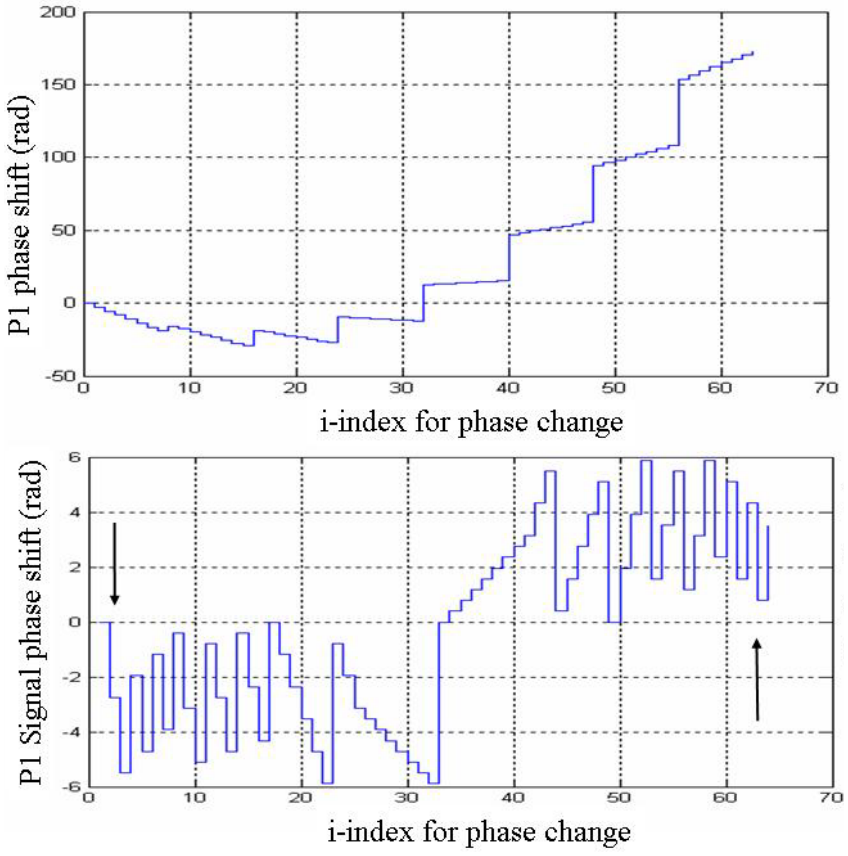

Figure 4. P1 Phase Shift and Unwrapped Phase Shift (radians) vs. Index for Phase Change.

D. POLYPHASE CODE P2

The P2 code has the same phase increments within each phase group as the P1, except that the starting phases are different [10]. The P2 code is given by [1]

$$\phi_{i,j} = \frac{-\pi}{2M}[2i-1-M][2j-1-M] \tag{2.9}$$

where i = 1, 2, 3… M, j = 1, 2, 3… M, and N_c is the number of phase codes

$$N_c = M^2 \tag{2.10}$$

where N_c=1,2,3…. The peak side lobe level is given by

$$PSL = 20\log_{10}(1/M\pi) \tag{2.11}$$

The phase shift and unwrapped phase shift for a P2 signal with M = 8, N_c = 64, f_c = 1 kHz, f_s = 7 kHz, and *cpp* = 1 is shown in Figure 5. The code change is largest for the P2 signal at the ends of the code (indicated by black arrows).

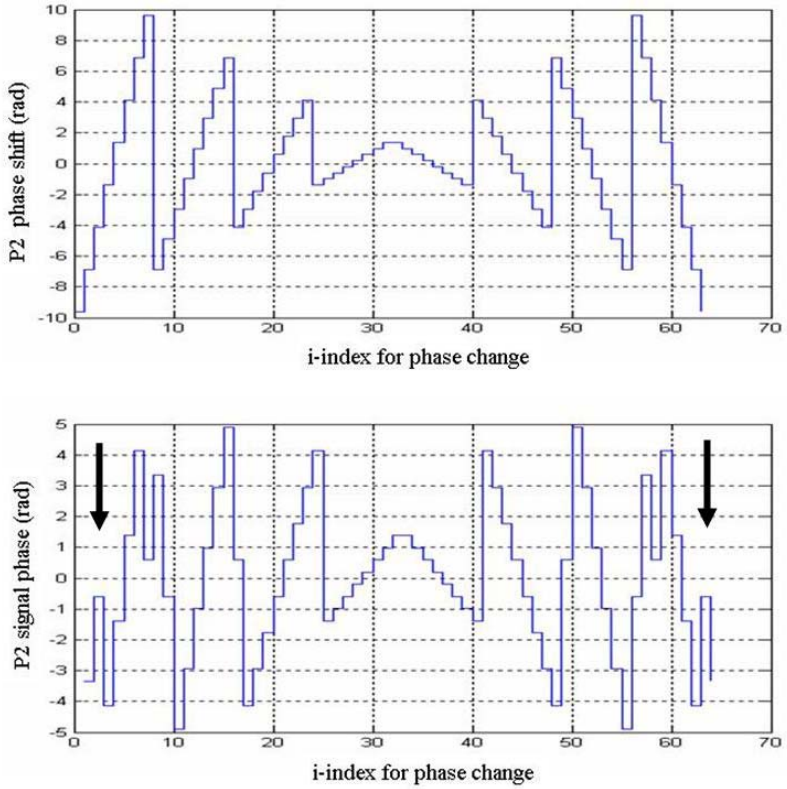

Figure 5. P2 Phase Shift and Unwrapped Phase Shift (radians) vs. Index for Phase Change.

E. POLYPHASE CODE P3

The P3 code is conceptually derived by converting a linear frequency modulation waveform to baseband by using a synchronous oscillator on one end of the frequency sweep (single sideband detection) and sampling the *I* and *Q* video at the Nyquist rate. The first sample of *I* and *Q* is taken at the leading edge of the waveform [1, 10]. The phase of the *i*th sample of the P3 code is given by [1]

$$\phi_i = \frac{\pi}{N_c}(i-1)^2 \tag{2.13}$$

where $i = 1, 2, \ldots, N_c$, and N_c phase codes are present. The peak side lobe level is given as

$$PSL = 20\log_{10}(\sqrt{2/(N_c\pi^2)}) \tag{2.14}$$

The phase shift and unwrapped phase shift for a pulse-compression waveform (P3 signal) with $M = 8$, $N_c = 64$, $f_c = 1$ kHz, $f_s = 7$ kHz, and $cpp = 1$ is shown in Figure 6. The code change is largest for the P3 signal at the middle of the code (indicated by a black arrow). From (2.14), the *PSL* is -24.9 dB.

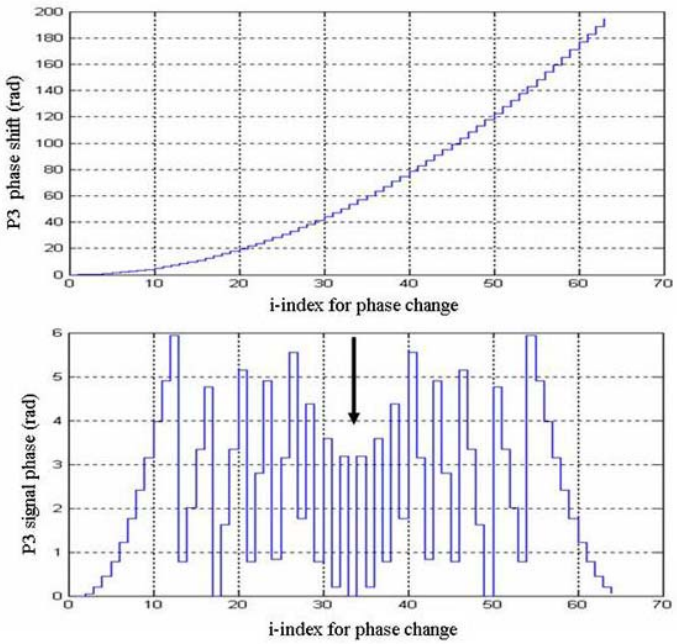

Figure 6. P3 Phase Shift and Unwrapped Phase Shift (radians) vs. Index for Phase Change.

F. POLYPHASE CODE P4

The P4 code is conceptually derived from the same linear frequency modulation waveform as the P3 code except that the local oscillator frequency is offset in the *I* and *Q* detectors, resulting in double sideband detection [1]. The phase sequence of the P4 signal is described by [6]

$$\phi_k = \frac{\pi}{N_c}(k-1)^2 - \pi(k-1) \tag{2.15}$$

where k = 1, 2, 3, ..., N_c, and N_c phase codes are present. The peak side lobe level is also given by

$$PSL = 20\log_{10}(\sqrt{2/(N_c\pi^2)}) \tag{2.16}$$

The phase shift and unwrapped phase shift for a P4 signal with M = 8, N_c = 64, f_c = 1 kHz, f_s = 7 kHz, and *cpp* = 1 is shown in Figure 7. The code change is largest for the P4 signal at the ends of the code (indicated by black arrows).

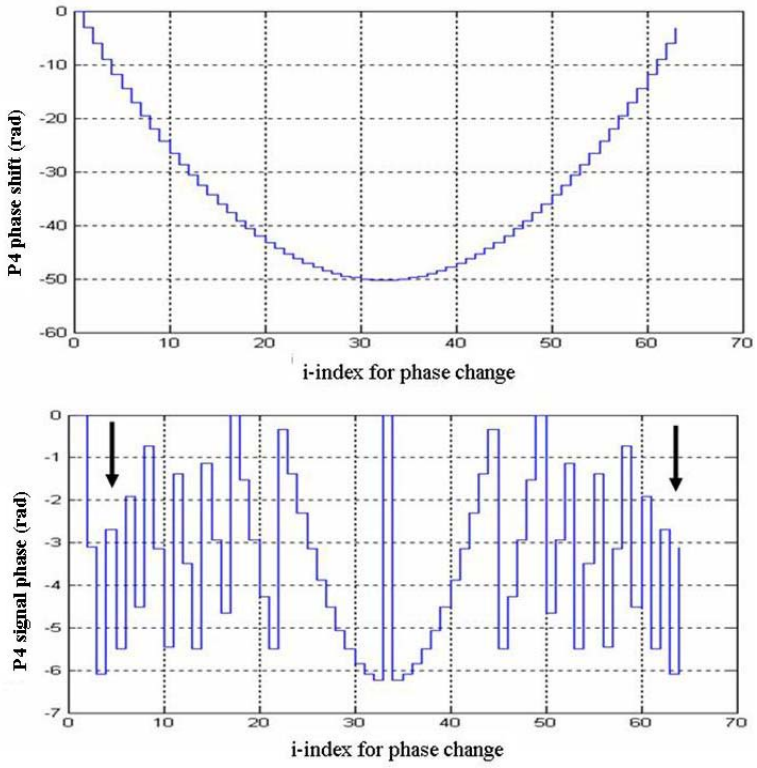

Figure 7. P4 Phase Shift and Unwrapped Phase Shift (radians) vs. Index for Phase Change.

G. POLYTIME CODE T1(*n*)

Polytime codes arise naturally from quantizing the accumulated phase of a stepped-RF waveform into a fixed number of evenly spaced phase states and requiring that no phase state be skipped in the process of encoding the underlying waveform; the T1(*n*) polytime sequence is generated with a stepped-RF waveform that is zero beat at the leading segment [2, 11]. In reference to polytime codes, *n* is the number of phase states used to approximate the underlying waveform [1, 6].

The equation for the wrapped phase, $\varphi(t)$, versus time for the T1(2) polytime sequence is [1, 2]

$$\varphi(t) = \mathrm{MOD}\left\{\frac{2\pi}{n}\mathrm{INT}\left[kt - jT\right], 2\pi\right\} \tag{2.17}$$

where j = 0, 1, 2, …, k-1 is the segment number in the stepped frequency waveform (RF waveform), k is the number of segments in the T1(2) code sequence, t is time, T is the overall code duration, and n is the number of phase states in the code sequence. The phase shift for a polytime code (T1(2) signal) with f_c = 1 kHz, f_s = 7 kHz is shown in Figure 8 and in Figure 9 the amplitude of the phase modulated carrier signal is shown against the corresponding time index.

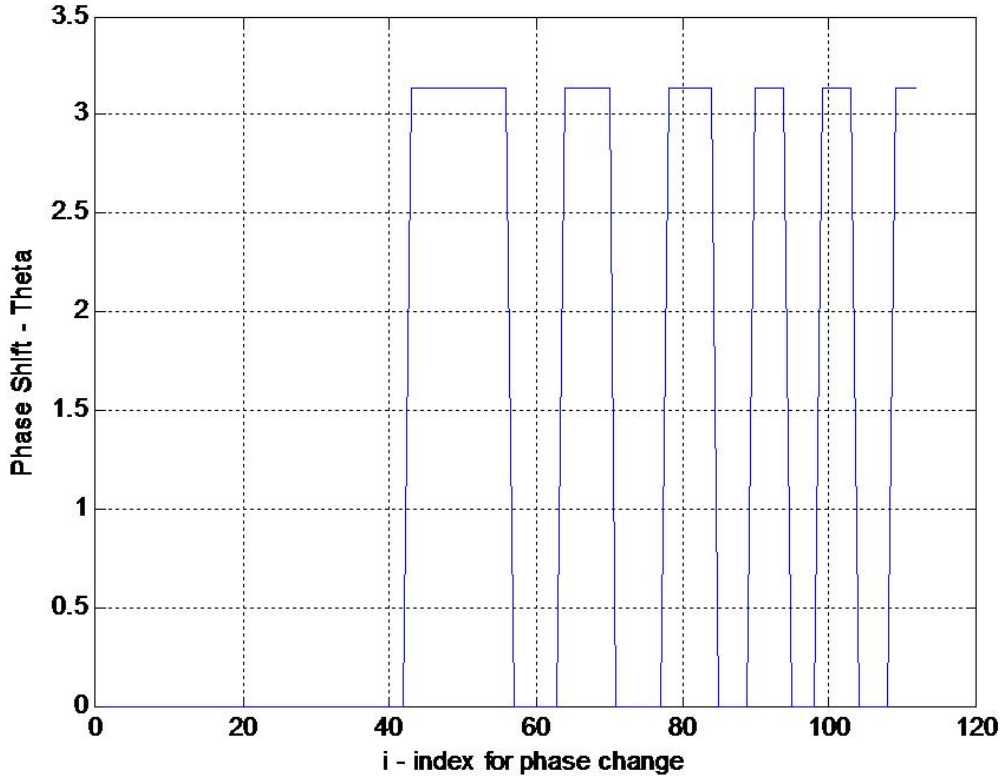

Figure 8. T1(2) Phase Shift (rad) vs. Index for Phase Change.

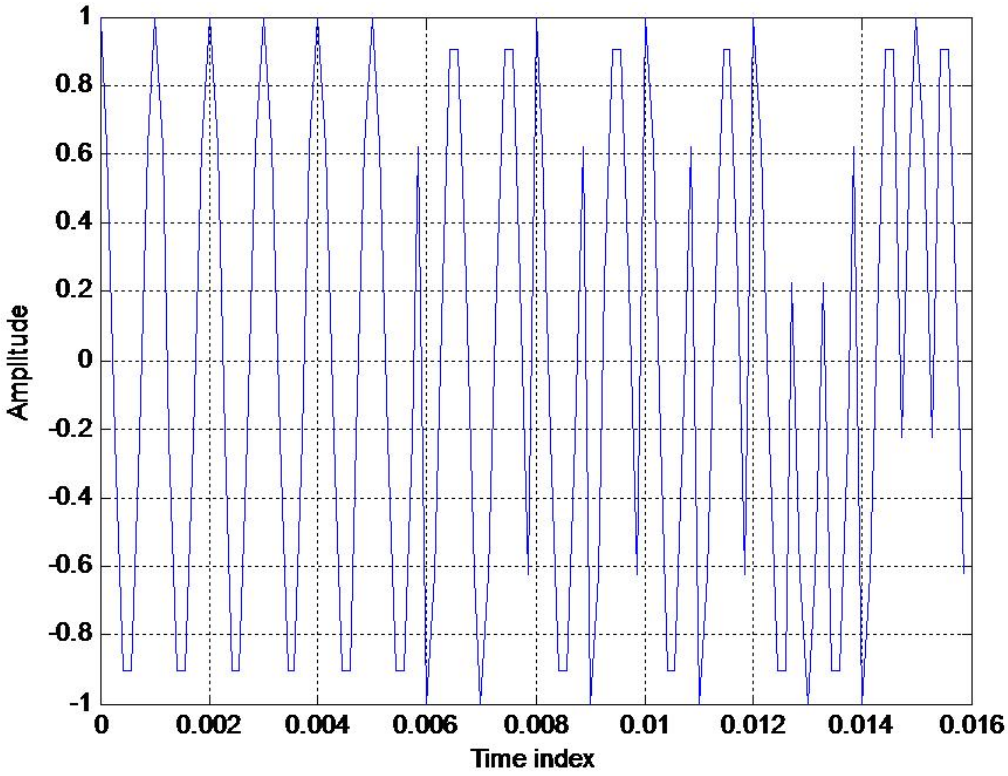

Figure 9. T1(2) Amplitude vs. Index for Phase Change.

H. POLYTIME CODE T2(*n*)

The T2(2) sequence is generated by approximating a stepped frequency waveform that is zero beat at the center frequency. If the stepped RF frequency has an odd number of elements, the zero beat frequency is the frequency of the center segment. If an even number of segments are used, the zero frequency is the frequency halfway between the two centermost segments. The expression for the wrapped phase versus time for the T2(2) polytime sequence is [1]

$$\varphi(t) = \mathrm{MOD}\left\{\frac{2\pi}{n}\,\mathrm{INT}\left[\left(kt - jT\right)\left(\frac{2j-k+1}{T}\right)\left(\frac{n}{2}\right)\right]\right\} \tag{2.18}$$

where j = 0, 1, 2, …, *k*-1 is the segment number in the stepped frequency waveform (RF waveform), *k* is the number of segments in the T2(2) code sequence, *t* is time, *T* is the overall code duration, and *n* is the number of phase states in the code sequence. The phase shift for a polytime code (T2(2) signal) with f_c = 1 kHz, f_s = 7 kHz is shown in Figure 10 and in Figure 11 the amplitude of the phase modulated carrier signal is shown against the corresponding time index.

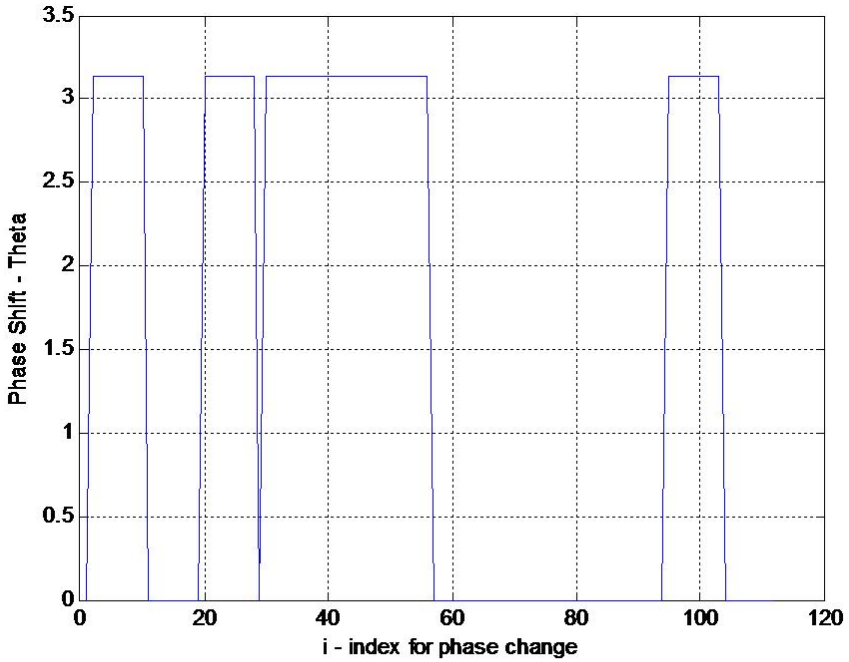

Figure 10. T2(2) Phase Shift (rad) vs. Index for Phase Change.

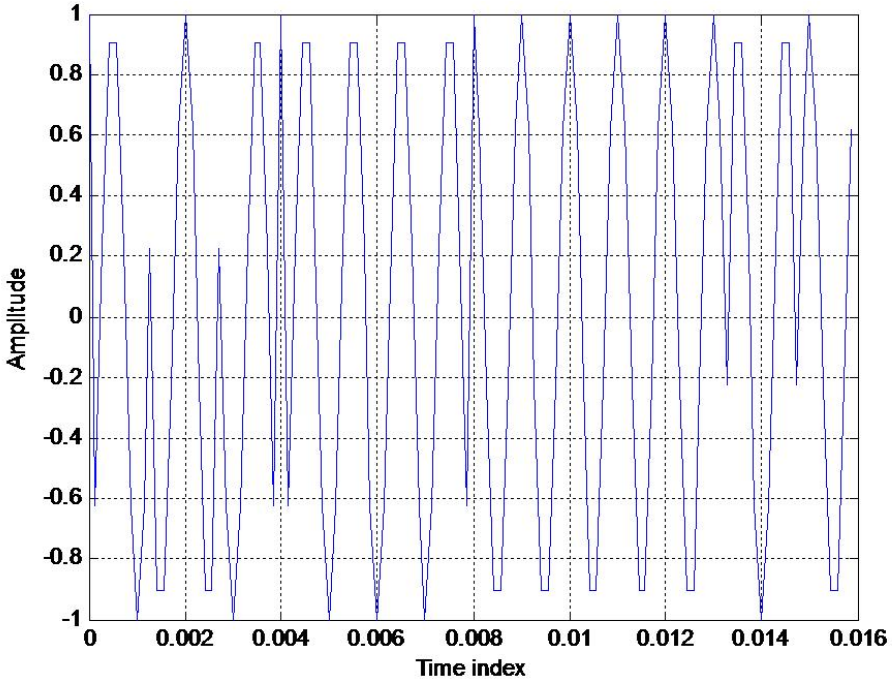

Figure 11. T2(2) Amplitude vs. Index for Phase Change.

I. BINARY PHASE SHIFT KEYING (BPSK)

In 1953, R. H. Barker presented binary sequences for synchronization purposes in telecommunications [1, 12]. It is important to not confuse Barker codes as LPI. Barker codes are not LPI because they are easily detected by an intercept receiver that uses frequency doubling [1]. Intercept receivers are also able to detect the large side lobes present in Barker codes. Barker codes result in a periodic ambiguity function with side lobe levels not higher than $20\log_{10}(1/N_c)$ dB relative to a main lobe level of 1 [1]. LPI signals are characterized by their small side lobes which prevent detection and reduce vulnerability to jamming. Barker codes are an important phase modulation technique that can be used to quantify the feature extraction and classification techniques presented in this thesis [1, 6]. Table 2 contains nine Barker codes with corresponding *PSL* and *ISL* [1].

Table 2. Nine Barker Codes with Corresponding *PSL* and *ISL*

Code Length	Code Elements	*PSL* (dB)	*ISL* (dB)
2	-+,-+	-6.0	-3.0
3	++-	-9.5	-6.5
4	++-+	-12.0	-6.0
4	+++-	-12.0	-6.0
5	+++-+	-14.0	-8.0
7	+++--+-	-16.9	-9.1
11	+++---+--+-	-20.8	-10.8
13	+++++--++-+-+	-22.3	-11.5

In the next chapter the time-frequency distributions used to detect the nine LPI radar modulations are presented. The time-frequency distributions are the Choi-Williams distribution, the Wigner-Ville distribution, and the Quadrature Mirror Filter Bank approach.

THIS PAGE INTENTIONALLY LEFT BLANK

III. TIME FREQUENCY DISTRIBUTIONS

In this chapter, three time-frequency analysis techniques are presented: Wigner-Ville distribution, Choi-Williams distribution, and the Quadrature Mirror Filter Bank.

A. WIGNER-VILLE DISTRIBUTION

The Wigner-Ville distribution has been applied in many areas of engineering to include optical implementations, medical applications, image analysis, target detection, and the analysis of nonstationary LPI signals [1]. The Wigner-Ville distribution is a powerful time-frequency analysis technique for signal processing, however, it does have drawbacks like interfering cross-terms between every pair of signal frequencies.

The implementation of the Wigner-Ville distribution used in this thesis was from [1, 2, 13]. The Wigner-Ville distribution of a continuous one-dimensional function $x(t)$ is defined as

$$W_{\chi}(t,\omega) = \int_{-\infty}^{\infty} x(t+\frac{\tau}{2})x^{*}(t-\frac{\tau}{2})e^{-j\omega t}d\tau \tag{3.1}$$

where *t* is the time variable, ω is the angular frequency variable, and the * indicates the complex conjugate. The Wigner-Ville distribution is a two-dimensional function describing the frequency content of a signal as a function of time [14].

The continuous time and frequency representation can be modified for a discrete sequence to achieve real-time evaluation. The discrete Wigner-Ville distribution is achieved by applying the continuous one-dimensional form of the distribution to a sampled time series $x(l)$, where *l* is a discrete time index from $-\infty$ to ∞. The discrete Wigner-Ville distribution is defined as

$$W(l,\omega) = 2\sum_{n=-\infty}^{\infty} x^{*}(l+n)x^{*}(l-n)e^{-2j\omega n} \tag{3.2}$$

windowing the data results in the pseudo-Wigner-Ville distribution gives

$$W(l,\omega) = 2\sum_{n=-N+1}^{N-1} x*(l+n)x^{*}(l-n)\omega(n)\omega(-n)e^{-2j\omega n} \tag{3.3}$$

where $\omega(n)$ is a length of $2N-1$ real window function with $\omega(0)=1$. Using $f_l(n)$ to represent the kernel function

$$f_l(n) = x(l+n)x^*(l-n)\omega(n)\omega(-n) \tag{3.4}$$

the pseudo-Wigner-Ville distribution becomes

$$W(l,\omega) = 2\sum_{n=-N+1}^{N-1} f_l(n)e^{-2j\omega n} \tag{3.5}$$

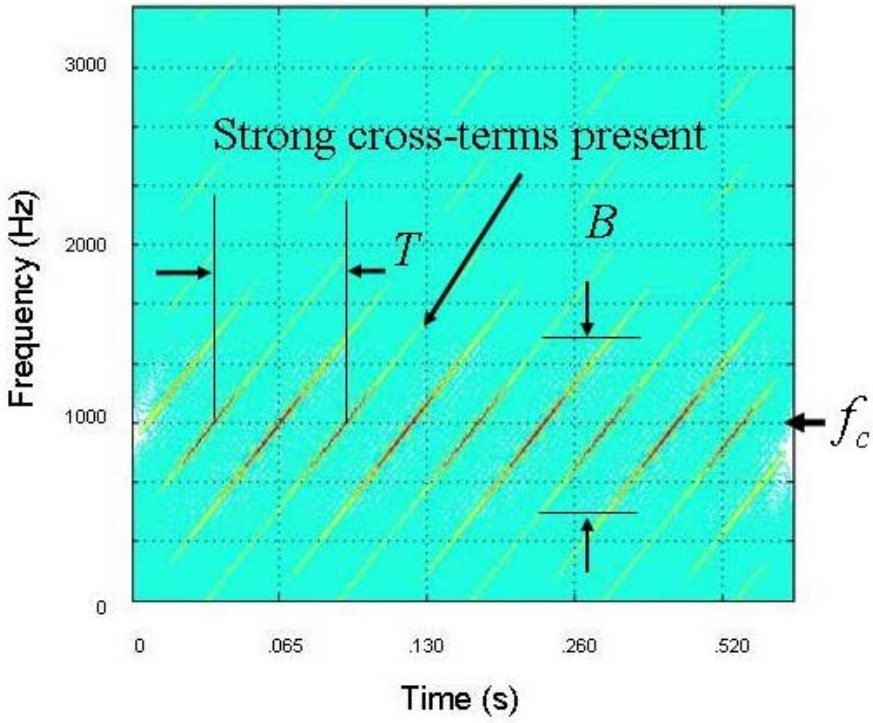

Figure 12. Wigner-Ville Distribution for a N_c = 64 Frank Signal.

Figure 12 shows the pseudo Wigner-Ville distribution for a N_c = 64 subcode Frank signal. Note the strong presence of cross-terms. Also note that the bandwidth, *B*, the carrier frequency, f_c, and the code period, *T*, can easily be measured.

B. CHOI-WILLIAMS

The Choi-Williams distribution simultaneously gives the representation of a signal in both time and frequency. It has been noted as one of the more useful in the Cohen's class of distributions since it reduces the amplitude of the cross-terms [6]. It is

hypothesized that reducing the cross-terms of the distribution results in better classification results.[1] The Choi-Williams distribution is given as [15]

$$C(t,\omega) = \iiint e^{j2\pi\xi(s-t)} f(\xi,\tau) x(s+\tau/2) x^*(s-\tau/2) e^{-j\omega\tau} d\xi ds d\tau \tag{3.6}$$

where

$$f(\xi,\tau) = \exp\left[\frac{(\pi\xi\tau)^2}{2\sigma}\right] \tag{3.7}$$

is a Gaussian parameterization function that controls the cross-terms and frequency resolution in the T-F image by varying σ. The reduced cross-terms are one of the advantages of using the Choi-Williams distribution over the Wigner-Ville distribution. Note that if the parameterization function is set to 1, $f(\xi,\tau)=1$, the result is the Wigner-Ville distribution.

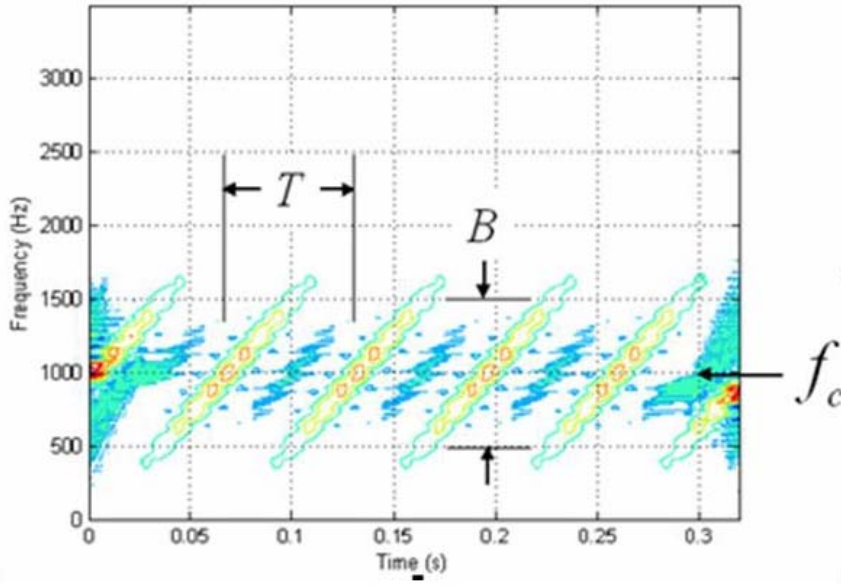

Figure 13. Choi-Williams Distribution for a N_c= 64 Frank Signal.

Figure 13 shows the Choi-Williams distribution for a N_c = 64 subcode Frank signal. Note the minimal cross-terms. Also note that the bandwidth, *B*, the carrier frequency, f_c, and the code period, *T*, can be easily measured.

1 In Chapter VIII, classification results are presented and this hypothesis is investigated.

C. QUADRATURE MIRROR FILTER BANK (QMFB) TREE

The Quadrature Mirror Filter Bank (QMFB) approach enables signal processing of LPI signals without having to take into consideration the effects of cross-terms. In distributions like the Wigner-Ville and Choi-Williams the presence of cross-terms makes the image noisy, which can sometimes give misleading results [1].

A QMFB tree is shown in Figure 14 and consists of a number of layers of fully connected pairs of orthogonal wavelet filters (or basis functions) that linearly decompose the received waveform into tiles on the time-frequency plane. By varying the wavelet size duration, resolution in time can be traded for resolution in frequency [2]. The frequency resolution of a QMFB layer *l* is

$$\Delta f = \frac{f_s}{2(2^l - 1)} \tag{3.8}$$

where f_s is the sampling frequency. The resolution in time is determined by how many samples are used within the QMFB and is

$$\Delta t = \frac{2^L}{f_s(2^{L-l} - 1)} \tag{3.9}$$

where *L* is the total number of layers.

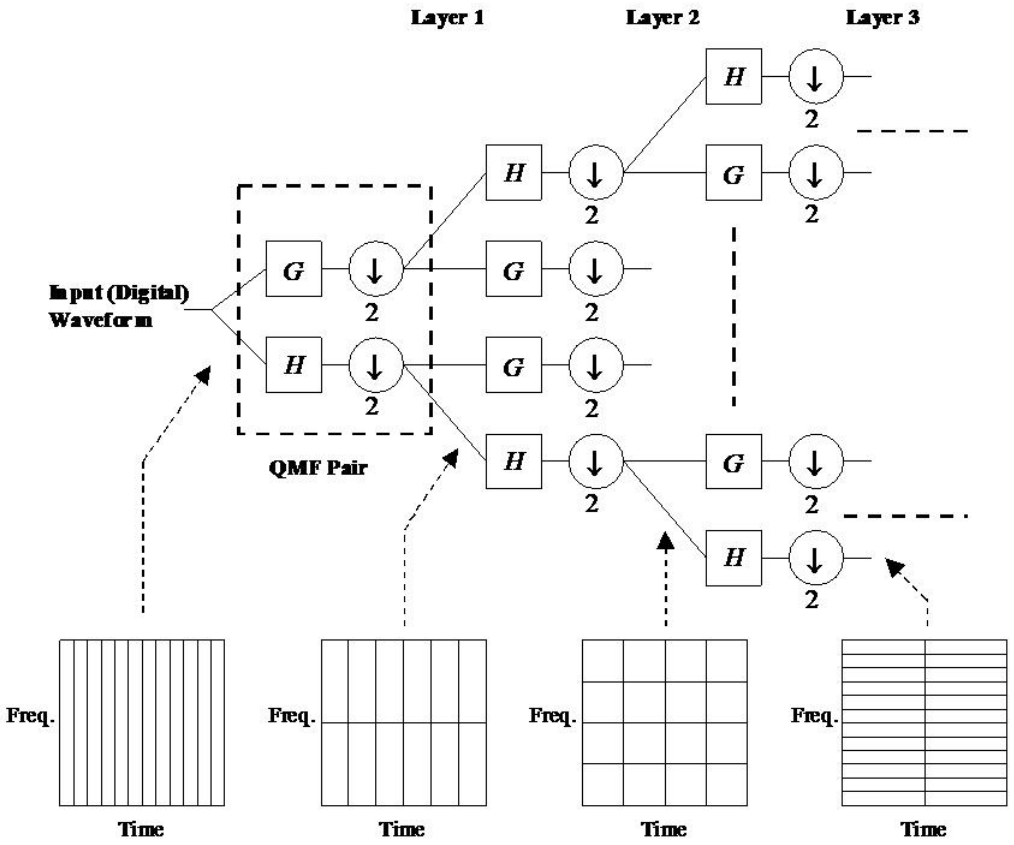

Figure 14. Quadrature Mirror Filter Bank (QMFB) Tree [1].

Figure 15 shows the QMFB distribution for layer 5 for a N_c = 64 Frank signal with *cpp* = 1, *T* = 64 ms, and *B* = 1 kHz. Note that the bandwidth, *B*, the carrier frequency, f_c, and the code period, *T*, can be easily measured. From (3.8 and 3.9) Δt = .005s and Δf = 112 Hz for this layer and represents a good trade-off in time-frequency resolution.

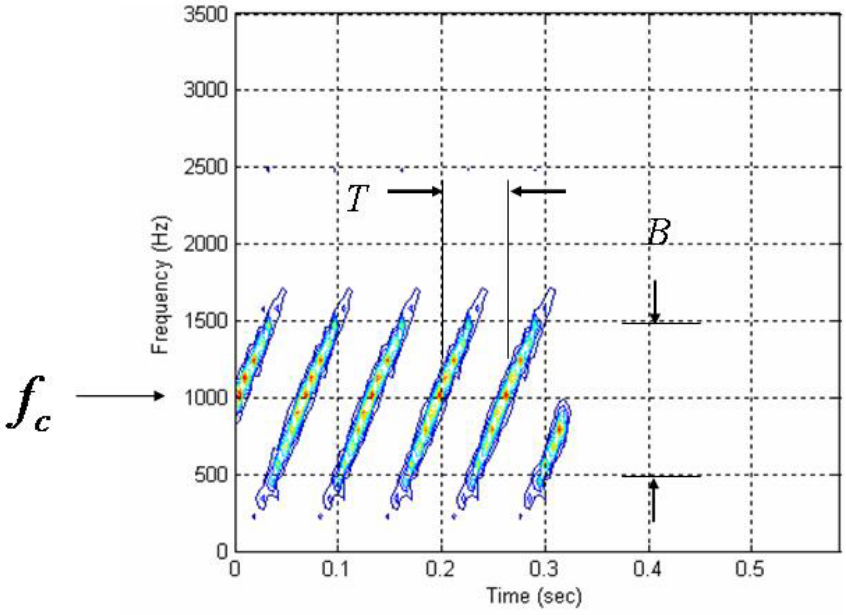

Figure 15. QMFB Layer 5 for a N_c=64 Frank Signal

In the next chapter, three feature-extraction algorithms are presented. These feature-extraction algorithms are applied to the nine LPI signals discussed in Chapter II from the three distributions discussed in this chapter.

IV. AUTONOMOUS CROPPING AND FEATURE EXTRACTION

In this chapter, the three autonomous cropping and feature extraction algorithms are presented. The first algorithm is the Erosion Dilation Adaptive Binarization (EDAB) process and involves a combination of two morphological operations (erosion and dilation) to isolate the modulation [16]. The second approach is called the Marginal Frequency Adaptive Binarization (MFAB) and uses the marginal frequency distribution to isolate the modulation [17]. The third approach uses Fourier and inverse Fourier transforms and Gaussian low-pass filters for modulation isolation [18].

A. EROSION DILATION ADAPTIVE BINARIZATION (EDAB)

A block diagram of the EDAB autonomous cropping and feature extraction image processing algorithm is shown in Figure 16. The LPI signal being shown to demonstrate the EDAB algorithm is the T1(2) shown in Figure 9. The first step of the algorithm is to remove the signal's no-signal region if it has one. A no-signal region in a LPI signal occurs if the duration of the LPI signal is smaller than the time interval processed. Since the no-signal region within the T-F image does not contain useful information for classification, this region is removed. The T1(2) signal with its no-signal region removed is shown in Figure 16. The image labeled as $C(t,\omega)$ is the LPI signal with the no-signal region present and the image labeled as $C'(t,\omega)$ is the same LPI signal with the no-signal region removed. Before the feature extraction processing, the image was resized (reduced by 0.1) using nearest neighbor interpolation in order to increase the processing speed (see Figure 16, No.1).

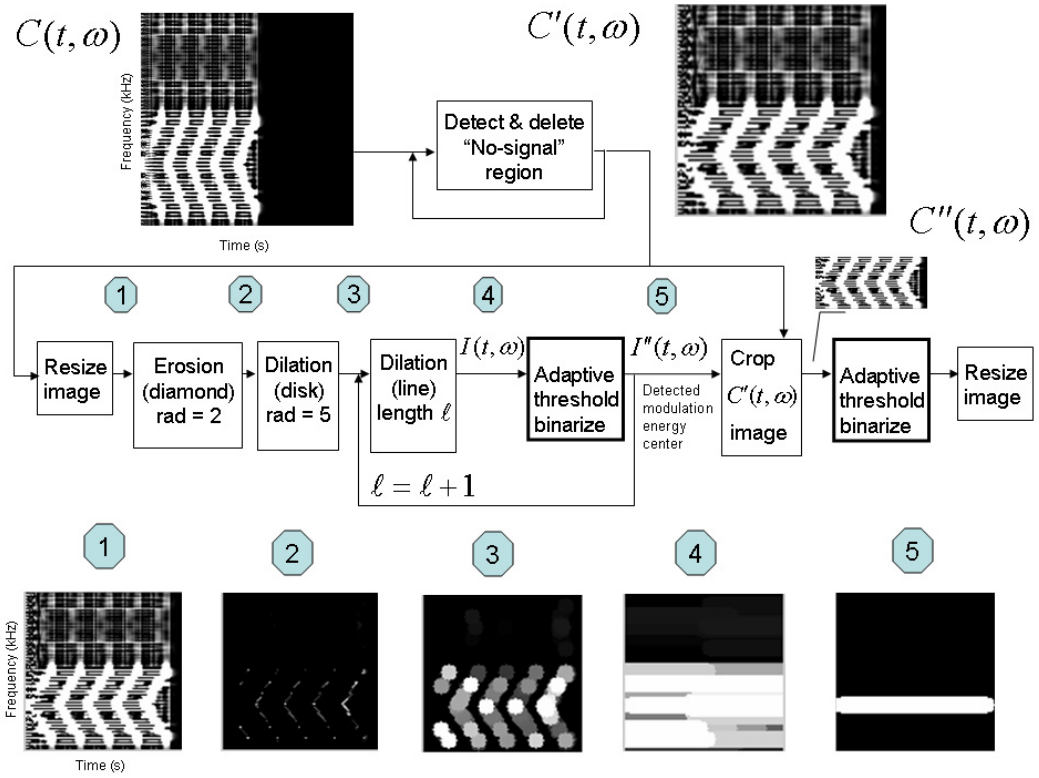

Figure 16. New Autonomous Feature Extraction Algorithm.

1. Erosion and Dilation Processing

Dilation and erosion are two functions that are fundamental to morphological operations [2]. In morphological dilation and erosion operations, the state of any given pixel in the output image is determined by applying a rule to the corresponding pixel and its neighbors (within a defined structuring element) in the input image [19]. The rule used to process the pixels defines the operation. For dilation, the output pixel is the maximum value of all the pixels in the input pixel's neighborhood. The dilation of image A by structuring element B, denoted $A \oplus B$, is defined as [2]

$$A \oplus B = \left\{ Z \mid (B)_z \cap A \neq \varnothing \right\} \tag{4.1}$$

where the dilation of A by B is the set Z consisting of all the structuring element origin locations where the reflected and translated B overlaps at some portion of A is not the empty set $\varnothing$ [18]. In terms of erosions and dilations the type of structuring element used depends on the need of the user.

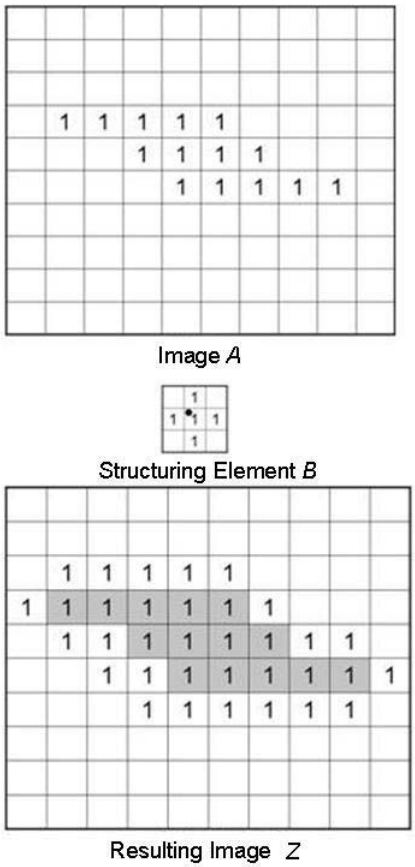

Figure 17. Sample Dilation.

Figure 17 demonstrates the dilation concept using a cross structuring element. When structuring element *B* is convolved with image *A* the resulting image is *Z* where the original pixels of the image are shaded in grey and those that are not shaded in grey are a result of the dilation. When the result of the AND operation between the reference pixel of the structuring element and the image *A* is 1 the pixels of the image are expanded to the shape of the structuring element.

For erosion, the value of the output pixel is the minimum value of all the pixels in the input pixel's neighborhood. The erosion of image *A* by structuring element *B*, denoted $A \ominus B$, is defined as [2]

$$A \ominus B = \left\{ Z \mid (B)_z \cap A^c \neq \varnothing \right\} \tag{4.2}$$

where the erosion of image *A* by structuring element *B* is the set *Z* of all structuring element origin locations where the translated *B* has no overlap with the background *A* and

is not the empty set ∅ [18]. Figure 18 demonstrates the erosion concept using a cross structuring element.

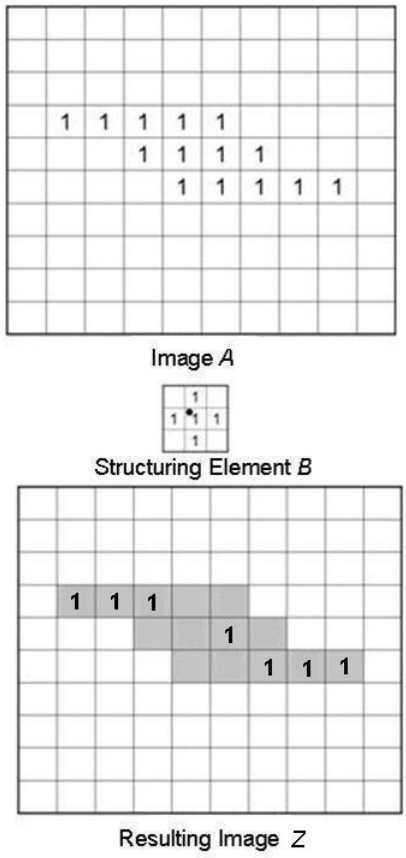

Figure 18. Sample Erosion.

When structuring element *B* is convolved with Image *A* the resulting image is *Z* where the original pixels of the image are shaded in grey. When the result of the AND operation between the reference pixel of the structuring element and the image is 1, the pixels of the image are deleted to the shape of the structuring element and only the pixel in Image *A* that is in the location that corresponds with the reference pixel of the structuring element remains a 1.

The first erosion operation in the EDAB algorithm uses a diamond structuring element with radius 2. Table 3 presents the different structuring elements used in the EDAB algorithm and a description of why that particular structuring element was chosen. Each structuring element is chosen strategically to accomplish a certain morphological task. The first erosion serves to detect the signal modulation and eliminate any noise

present in the image. This process is shown in more detail in Figure 19. The erosion output clearly detects the T1(2) modulation in this example. The erosion operation is followed by a dilation operation (disk structuring element with radius 5) to enhance the detected modulation features within the image (see Figure 16, No. 3).

Table 3. Structuring Elements Used in EDAB Algorithm

Structuring Element	Description
Diamond 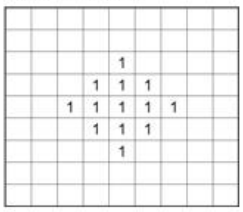	The diamond structuring element is used to eliminate noise
Disk 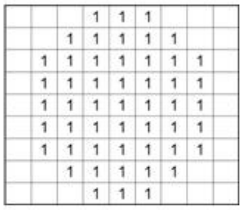	The disk structuring element is used to highlight the modulation energy
Line 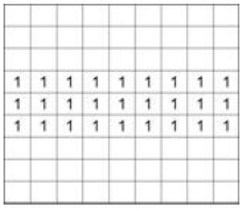	The line structuring element is used to expand the extracted modulation features across the time axis (horizontal axis) until there is a continuous line that runs across the length of the image

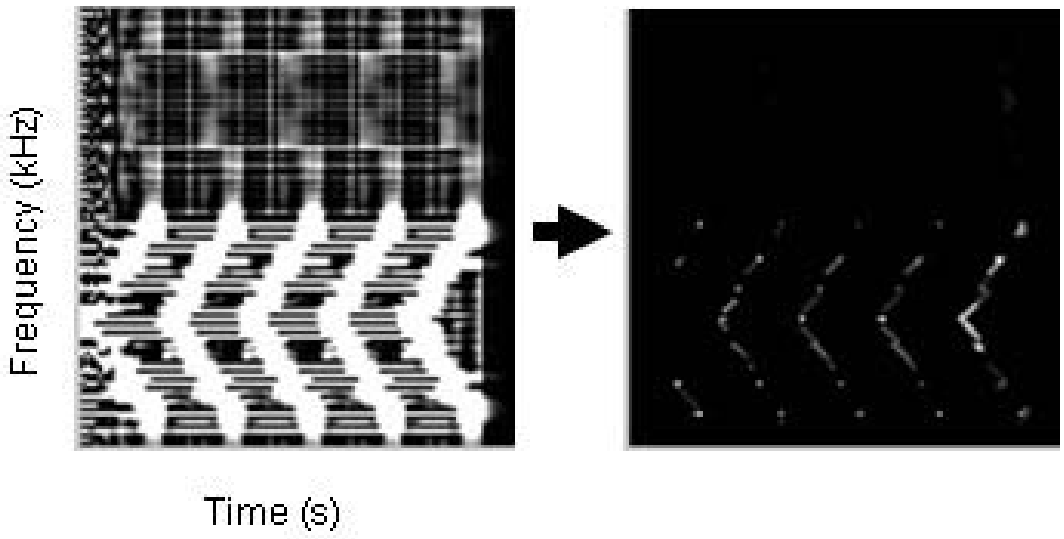

(a) (b)

Figure 19. Modulation Detection Process Showing the (a) Resized Image and (b) Erosion Output.

The erosion and dilation are followed by a recursive dilation operation (line structure with length *l*) [20]. The recursive dilation operation expands the extracted modulation features along the time axis (pixels aligned horizontally) until a continuous strip results. The increment *l* is used to control the length of the horizontal structuring element to ensure that the output of the dilation is an image with a *continuous* horizontal line that runs the length of the entire image. The initial length is set to 0 and incremented as $l = l + 1$. The dilation output results are shown in Figure 20(a). Embedding the dilation operation in a feedback loop about an adaptive threshold binarization process then allows the detection of the modulation energy center as shown in Figure 20(b).

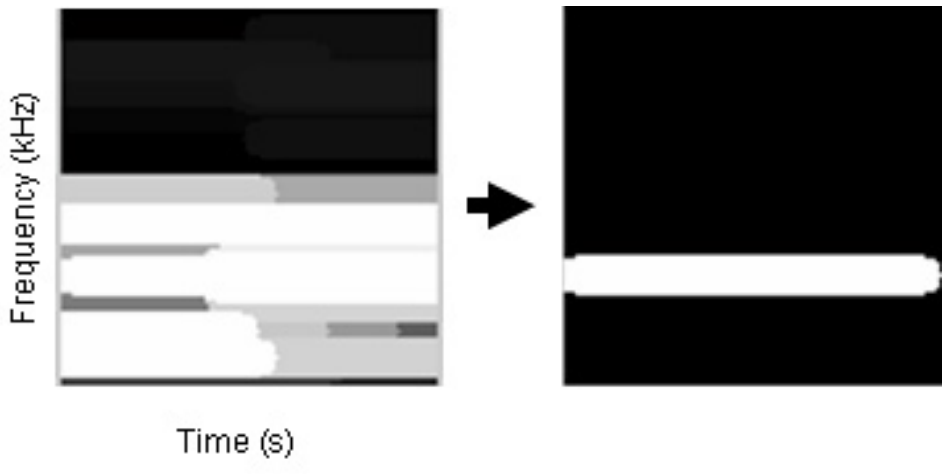

(a) (b)

Figure 20. Energy Center Detection Showing (a) Dilation Output and (b) Modulation Energy Center Detected.

2. Adaptive Threshold Binarization Processing

A block diagram of the adaptive threshold binarization process is shown in Figure 21. The intensity image $|I(t,\omega)|$ is normalized $I'(t,\omega)$ with respect to the largest value in the image, where the pixel values $0 \le I'(t,\omega) \le 1$.

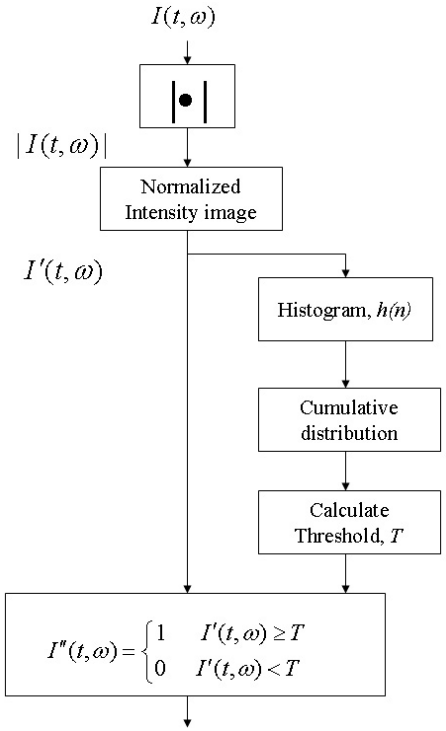

Figure 21. Adaptive Threshold Binarization Process.

A histogram of the intensity level content, $h(n)$, is then generated using $N = 50$ bins. The cumulative distribution function is computed using this histogram as

$$cdf(n) = \frac{\sum_{i=1}^{n} h(i)}{\sum_{n=1}^{N} h(n)} \tag{4.3}$$

A *cdf* threshold, *C*, is chosen and the intensity bin *n* where $cdf(n) \geq C$ is then identified. For example, if the *cdf* threshold is chosen experimentally to be *C* = 0.8, this means that only 20% of the brightest pixels above the threshold are retained. With this intensity bin, a corresponding normalized intensity threshold, *T = n/N*, is calculated. This threshold is then used to convert the intensity image into a binary image. That is,

$$I''(t,\omega) = \begin{cases} 1 \text{ (black)} & I'(t,\omega) \geq T \\ 0 \text{ (white)} & I'(t,\omega) < T \end{cases} \tag{4.4}$$

which effectively removes much of the noise and weak interference.

3. Autonomous Cropping and Final Image Resize

After the signal modulation energy center is identified, the information is used to autonomously crop the modulation pixels from the original image $C'(t,\omega)$ (shown in Figure16) to form the image shown in Figure 22(b).

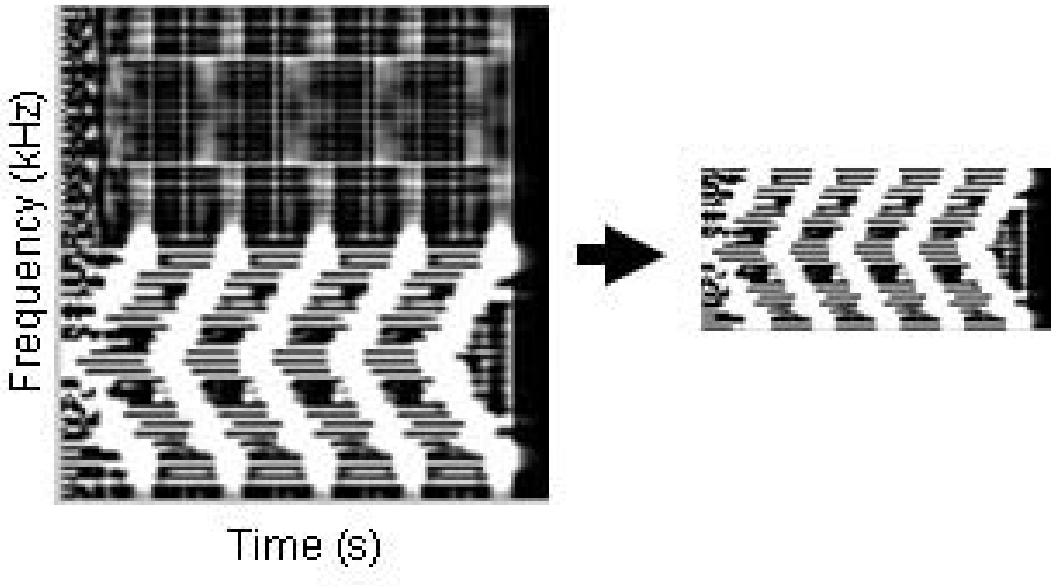

(a) (b)

Figure 22. Autonomous Cropping Showing (a) Original Resized Image and (b) Cropped Image.

The adaptive threshold binarization algorithm is used again to generate a binary feature image. Since the information is binary, the image is resized to $N'_r \times N'_c$ by low pass filtering, resampling and then applying a bilinear interpolation. The low pass filter is used to reduce the effect of *Moire'* patterns and ripple patterns that result from aliasing during the resampling operation [21]. The $N'_r \times N'_c$ image is then converted into a *feature vector* of size $N'_r \times N'_c \times 1$ for processing by a multi-layer perceptron classification network where $N'_r = N'_c = 50$.

B. MARGINAL FREQUENCY ADAPTIVE BINARIZATION (MFAB)

A block diagram of the autonomous feature extraction image processing is shown in Figure 23. The LPI signal shown to demonstrate the MFAB algorithm is the T1(2). Since the no-signal region within the T-F image does not contain useful information for classification, this region is removed. An LPI signal (T1(2)) with its no-signal region removed is shown in Figure 24.

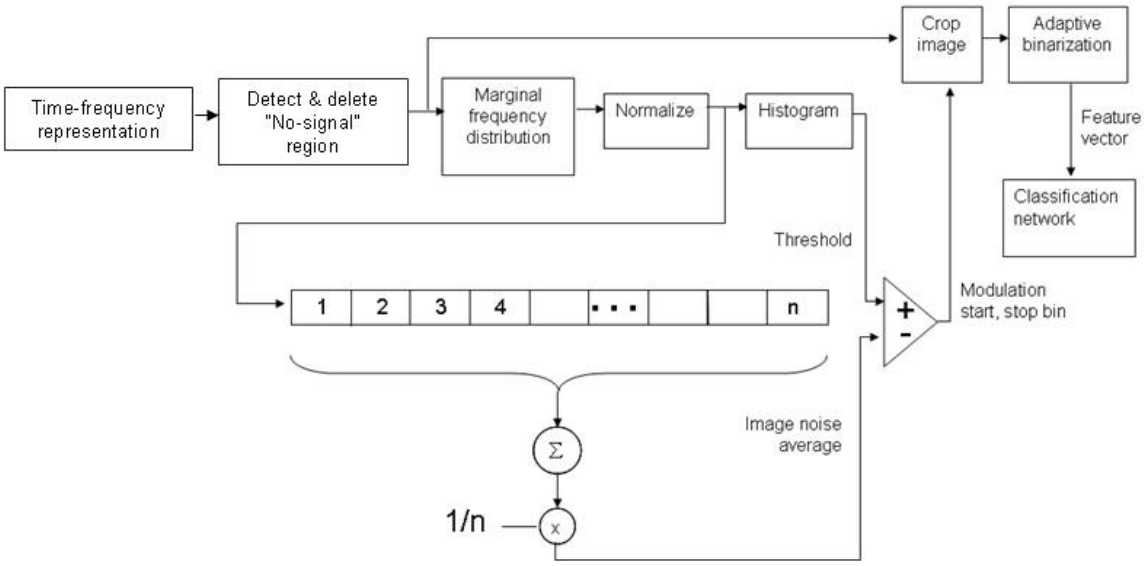

Figure 23. Autonomous Preprocessing to Isolate Signal Modulation

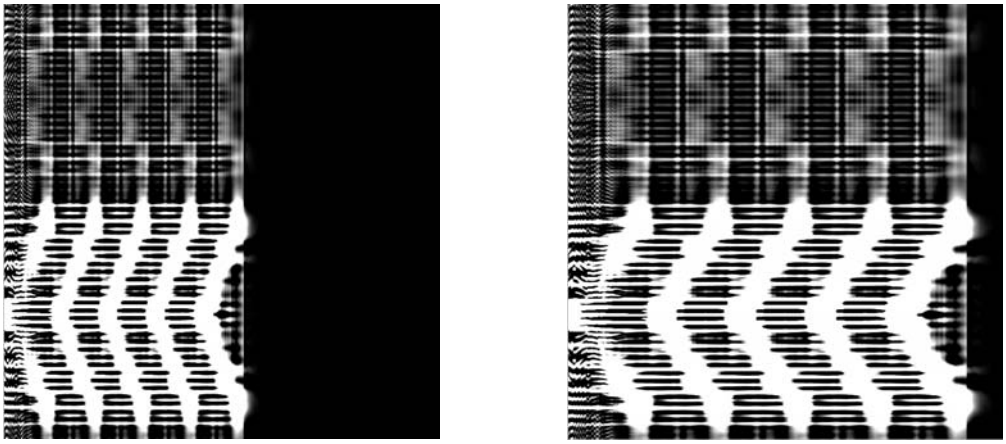

(a) (b)

Figure 24. T-F Image Showing (a) No-Signal Region and (b) the Same Image with No-Signal Region Extracted.

1. Marginal Frequency Distribution

The marginal frequency distribution offers one way to examine a T-F image in cases where there is a low SNR [22]. The marginal frequency distribution gives the instantaneous energy of the signal as a function of frequency. LPI signals have a low SNR and that is why using a marginal frequency distribution for analysis produces optimum results. The marginal frequency distribution is generated by

$$C(\omega) = \int C(t, \omega) dt \tag{4.5}$$

or summing the time values for each frequency in the T-F image and then storing the sums in an array. Each marginal frequency distribution is a unique representation of the T-F image it was generated from. The marginal frequency distribution is normalized by dividing the sums by the largest sum in the array. The normalized marginal frequency distribution of the T1(2) signal, shown in Figure 24, is shown in Figure 25.

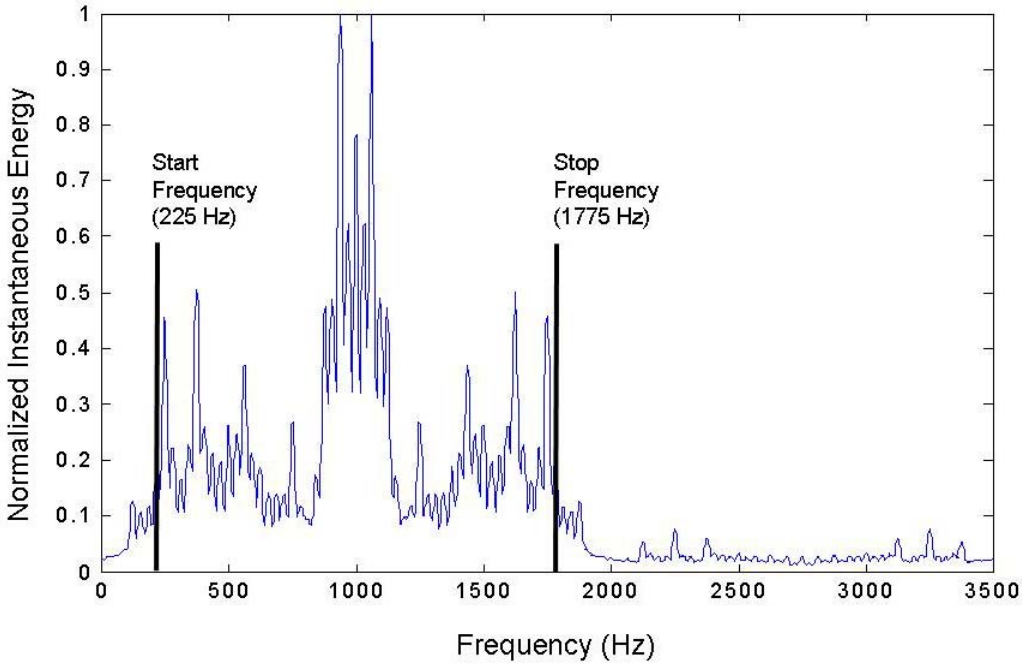

Figure 25. Normalized Marginal Frequency Distribution of the T1(2) Image Shown in Figure 24.

The normalized distribution is used to extract a threshold that is used later to isolate and crop the modulation energy within the T-F image. The threshold is determined by generating a histogram of 100 bins of the normalized marginal frequency distribution and then taking the value from the histogram bin which generates the best probability of correct classification (Pcc) results and initializing that value as the threshold. An example of the T1(2) histogram is shown in Figure 26.

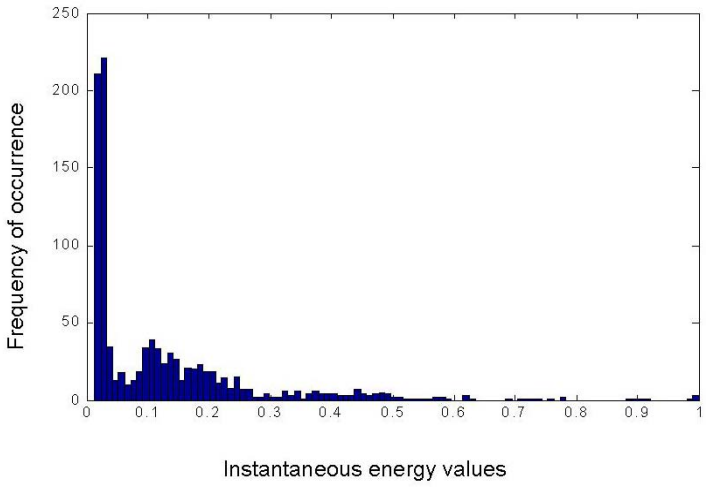

Figure 26. Histogram of the Normalized Marginal Frequency Distribution (T1) Used to Determine Threshold Autonomously.

Once the threshold is determined, the convolution of the averaging kernel (n = 9) and the normalized marginal frequency distribution is used to determine the start and stop location of the modulation energy. The convolution operation calculates the mean of the corresponding cells in the normalized distribution and compares it to the threshold identified from the histogram. If the average of the convolution is greater than the threshold, the start of the modulation energy is found. To find the stop location the same convolution algorithm is used but the kernel is initialized at the end of the normalized distribution. With the location of the modulation energy known, it can be cropped from the T-F image.

2. Autonomous Cropping

After the location of the signal modulation energy is identified, the information is used to autonomously crop the modulation pixels from the original image shown in Figure 27(a) to form the new image shown in Figure 27(b).

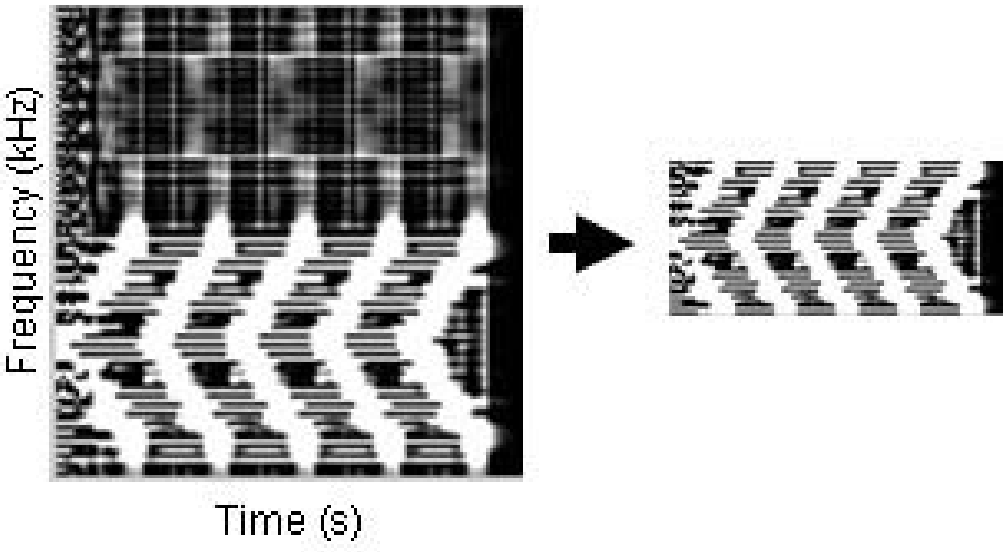

(a) (b)

Figure 27. Autonomous Cropping Showing (a) Original Resized Image and (b) Cropped Image.

3. Final Image Resize

The binarized image is resized to $N'_r \times N'_c$ by low pass filtering, resampling and then applying a bilinear interpolation. The low pass filter is used to reduce the effect of *Moire'* patterns and ripple patterns that result from aliasing during the resampling operation [21]. The $N'_r \times N'_c$ image is then converted into a *feature vector* of size $N'_r \times N'_c \times 1$ for processing by the multi-layer perceptron classification network where $N'_r = N'_c = 50$.

C. FAST FOURIER TRANSFORM (FFT) IMAGE FILTERING

The fast Fourier transform (FFT) is a powerful variation of the Fourier transform because of its ability to be applied to algorithms that require real-time processing. In an operational environment, LPI signals need to be processed and classified expeditiously. Figure 28 shows the block diagram of the 2D FFT process. Before the 2D FFT is applied to the image it needs to be preprocessed. Preprocessing can include any morphological operations to the image that are needed to continue with the algorithm. After any necessary preprocessing, the 2D FFT can be applied to the image. The 2D FFT is defined as

$$X(k_1,k_2)=\sum_{n_1=0}^{N-1}\sum_{n_2=0}^{N-1}x(n_1,n_2)e^{-2j\pi(k_1n_1+k_2n_1)/N} \tag{4.6}$$

where

$$0\le k_1,k_2\le N-1 \tag{4.7}$$

The 2D FFT is computed by computing the 2D FFT on all of the rows and all of the columns of the image being processed [23]. The image is then filtered in the frequency domain with a Gaussian low-pass filter; the Gaussian low-pass filter only allows areas of low frequency to pass and prevents high frequency noise from passing. The assumption is that, in a LPI signal, the modulation energy is low frequency and any noise would be high frequency. The output of the convolution should only be the modulation energy of the LPI signal in the frequency domain. The resulting image is then taken back to the time domain with an inverse 2D FFT. The resulting image shows the modulation energy of the LPI signal [18]. After the inverse 2D FFT is applied, the image is post-processed with any necessary morphological operations that might be required to conclude the algorithm.

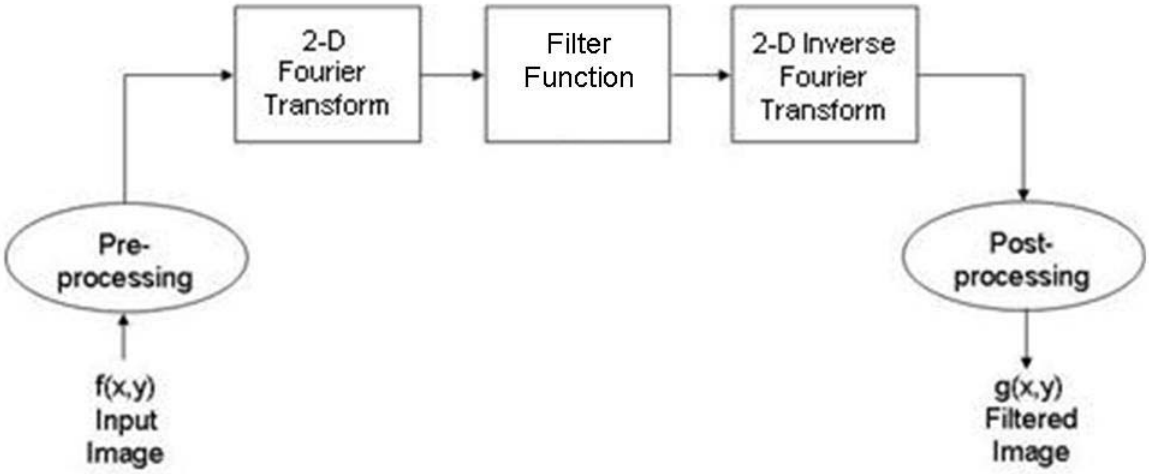

Figure 28. Theoretical Fourier Transform Processing [18].

Figure 29 shows a sample output out of the fast Fourier algorithm using a T1(2) signal. Figure 29(a) is the T1(2) signal. After the 2D Fourier transform and the Gaussian low-pass filter with a standard deviation of 10 were applied to the signal (Figure 29(b) and Figure 29(c)) the inverse 2D Fourier transform was applied and the output was the LPI signal with the modulation energy present and much of the noise removed. Ideally,

all the noise would be removed from the image and the output of the inverse 2D FFT would be an image containing only the modulation energy that could be used as an input as a feature vector into a classification network. Figure 29(d) contained enough noise that the image itself could not be used as a feature vector into a classification network. Post-processing actions would need to be applied to the image in order for it to be a suitable input into a classification network.

The Fast Image Filtering technique can not be used by itself as an algorithm to process an LPI signal for input into a classification network. However, this algorithm can be combined with any of the other two algorithms presented in this chapter to do so. The Fast Image Filtering technique can be a tool to eliminate noise from the image before any of the other algorithms are applied.

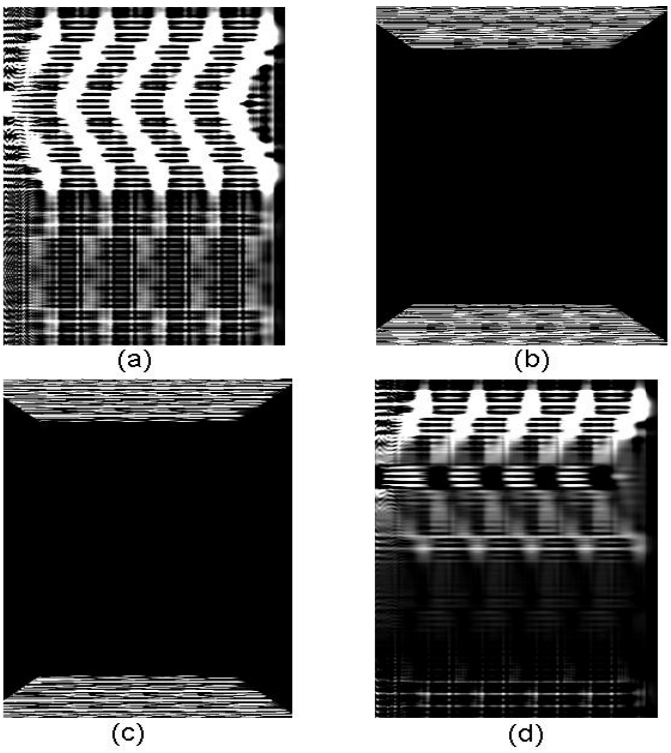

Figure 29. Sample LPI Signal Output from Fourier Algorithm.

In the next chapter the three databases of signals are described. Three databases were developed that contain LPI signals to test the feature extraction algorithms and classification networks presented in this thesis.

THIS PAGE INTENTIONALLY LEFT BLANK

V. DATABASE DESCRIPTION

The database used in the detection, feature-extraction, and classification process of LPI signals is an important point to consider when attempting to generate results that can emulate the results from an operational environment. Classification results will be more accurate if the database of LPI signals resembles signals found in the real-world.

Three databases, generated by Professor Phillip Pace from the Naval Postgraduate School, are investigated in this thesis. The first database consists of LPI signal modulations at a single carrier frequency of 1 kHz (BPSK, FMCW, Frank, P4, T1(2)). To train the classification network 56 signals were used. Twenty signals with modulation variations and 90 signals with noise variations (SNR = 1, 2, 3, -1, -2) were used to test the classification network. A second, more diverse, database was generated that contained signals at two different carrier frequencies (1 kHz and 2 kHz). From this database 144 signals were used in the training of the classification network. To test the classification network 46 signals with modulation variations and 180 signals with noise variations (SNR = 1, 2, 3, -1, -2) were used. Table 4 illustrates the modulation parameters for the first and second database. In the table, the column that describes the original parameters of the signals is symbolic of the signals used to train the classification networks and the column that describes variation is symbolic of the signals used to test the classification networks. A database that contains signals at multiple carrier frequencies is one step closer to generating a database that mimics the operational environment.

Table 4. Second Database Used for Detection/Feature Extraction/Classification

SIGNAL	Original Parameters	**Variation in Modulation Parameters**	Description of Modulation Parameters
BPSK			
cpp (Hz)	1,4,7	2,3,5,6	Carrier cycles per subcode
Nc	7,11	7,11	Number of subcodes
f_c (kHz)	1,2	1,2	Carrier frequency*
FMCW			
ΔF (Hz)	250,500	350,450	Modulation bandwidth
t_m (msec)	20,50	35,45	Modulation period
f_c (kHz)	1,2	1,2	Carrier frequency*
FRANK			
cpp (Hz)	1,4,7	2,3,5,6	Carrier cycles per subcode
N_c	16	16	Number of subcodes
f_c (kHz)	1,2	1,2	Carrier frequency*
P4			
cpp (Hz)	1,4,7	2,3,5,6	Carrier cycles per subcode
N_c	16	16	Number of subcodes
f_c (kHz)	1,2	1,2	Carrier frequency*
T1			
n	2,6	3,4,5	Number of phase states
k	4	4	Number of code segments
f_c (kHz)	1,2	1,2	Carrier frequency*

The third database was the most diverse of the three. It contained signals at two different carrier frequencies (1 kHz and 2 kHz) with multiple SNRs (SNR = -10 dB to 10 dB). To train the classification network, 439 signals were used and to test the classification network, 638 signals were used. Table 5 illustrates the modulation parameters for the third database. This database mimics the operational environment even closer, and also provides the most complex database of the three presented to test the autonomous feature extraction algorithms discussed in this thesis. It contains BPSK, FMCW, Frank, P1, P2, P3, P4, T1(2), and T2(2) signals.

Table 5. Third Database Used for Detection/Feature Extraction/Classification

SIGNAL	Original Parameters	**Variation in Modulation Parameters**	Description of Modulation Parameters
BPSK			
cpp (Hz)	1,4,7	3,5	Carrier cycles per subcode
Nc	7,11	7,11	Number of subcodes
f_c (kHz)	1,2	1,2	Carrier frequency*
FMCW			
ΔF (Hz)	250,500	350,450	Modulation bandwidth
t_m (msec)	20,50	35,45	Modulation period
f_c (kHz)	1,2	1,2	Carrier frequency*
FRANK			
cpp (Hz)	1,4,7	3,5	Carrier cycles per subcode
N_c	16	16	Number of subcodes
f_c (kHz)	1,2	1,2	Carrier frequency*
P1-P4			
cpp (Hz)	1,4,7	3,5	Carrier cycles per subcode
N_c	16	16	Number of subcodes
f_c (kHz)	1,2	1,2	Carrier frequency*
T1, T2			
n	2,6	3,5	Number of phase states
k	4	4	Number of code segments
f_c (kHz)	1,2	1,2	Carrier frequency*

The next chapter describes the two classification networks used (MLP and RBF) to classify the different LPI signals after they have been processed by the feature extraction algorithms.

THIS PAGE INTENTIONALLY LEFT BLANK

VI. CLASSIFICATION

A. MULTI-LAYER PERCEPTRON (MLP)

To classify the signal modulations, a multi-layer perceptron was used with 2 hidden layers and an output layer as shown in Figure 30. Hidden layer one contained N_1 neurons and hidden layer two contained N_2 neurons. Each neuron contained an activation function which could be logsig $(1/1+e^{-n})$, tansig $(2/1+e^{-2n}-1)$, or purelin (n). The output layer contained N_o neurons (one for each modulation).

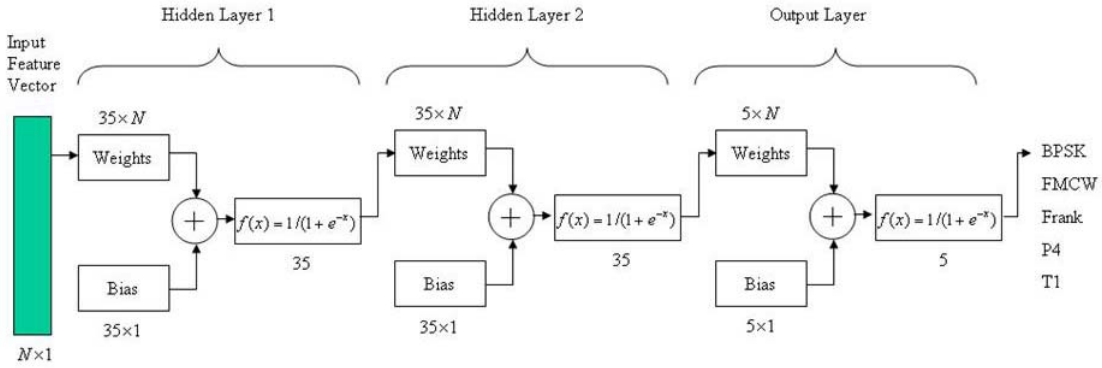

Figure 30. Three-layer Perceptron Used for Classification.

MLPs are capable of quickly learning nonlinear functions however they may exhibit poor generalization ability [24]. Therefore, The MLP used for classification to test the feature extraction algorithms used an improved generalization using regularization R

$$R = aMSE + (1-a)MSW \tag{6.1}$$

where a is the performance parameter, MSE is the mean square error between desired and network generated output, and MSW is the mean sum of squares of the network weights and biases. The following are characteristics of the MLP used to classify and test the feature extraction algorithms of this thesis:

- Hidden unit representations of MLP depend on weighted linear summations of inputs transformed by monotonic activation functions.

- Activation of hidden unit is constant on surfaces consisting of 1-D hyperplanes on 2-D input space.
- Distributed representation in activation space.
- Many layers of weights and complex pattern connectivity.
- All parameters in MLP determined at same time in a single global (non-linear) training strategy involving supervised learning.

B. RADIAL BASIS FUNCTION (RBF)

The Radial Basis Function (RBF) is the other classification network used to classify the different signal modulations. A RBF network usually consists of three layers, as shown in Figure 31. The first layer is the input layer and is made up of source nodes. The second layer is a hidden layer of high dimension, providing a set of functions that constitute an arbitrary basis for the inputs when they are expanded into the hidden-unit space. These functions are called the radial basis functions. The output layer supplies the response of the network to the activation patterns applied to the input layer [25].

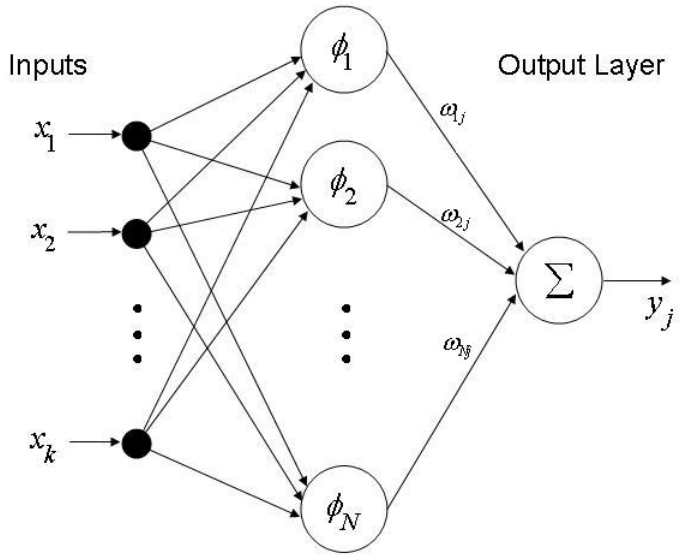

Figure 31. RBF Used For Classification Showing Input, Hidden, and Output Layer.

In the RBF, the relationship between the input and output is given by

$$f(x) = \sum_{n=1}^{N} \omega_n \phi_n(\| x - c_n \|) \tag{6.2}$$

where $\phi_n(\| x - c_n \|)$ is the Euclidean distance of the input vector x from a center c_n. The vectors c_n, (n = 1, …, N), are referred to as the centres of the basis functions and ω_n (n = 1, …, N) are the synaptic weights [25, 26]. In this thesis, the Gaussian form of the RBF was used. In the Gaussian form

$$\phi_n(\| x - c_n \|) = e^{\frac{-\|x-c_n\|^2}{\sigma^2}} \tag{6.3}$$

to give

$$f(x) = \sum_{n=1}^{N} \omega_n e^{\frac{-\|x-c_n\|^2}{\sigma^2}} \tag{6.4}$$

The Gaussian form contains the variable for spread (σ), or the width parameter, which is used in Chapter VII to optimize the RBF network.

The characteristics of the RBF used to classify and test the feature extraction algorithms of this thesis are:

- Hidden units in RBF network use distance vector between input and basis function centers followed by transformation with localized function.
- Activation of basis function is a constant 1D hyperellipsoids in 2D input space.
- Localized basis (Gaussian) functions form representation in activation space that is local with respect to input space.
- Simple architecture consisting of two layers:
    - First layer: Parameters of basis function.
    - Second layer: Linear combinations of basis function activations.
- Trained in two stages:
    - Basis functions determined by unsupervised techniques using input data.

    - Second layer weights found by fast linear supervised method.

- Best spread (or width) parameter σ is determined in training.
- Training is fast and efficient.

In the next chapter an investigation of the MLP and RBF is done. The MLP is optimized as a function of the number of neurons in the hidden layers, activation function, and performance goal. The RBF is optimized as a function of the spread value, σ. Classification results for the different settings of the classification networks are presented.

VII. SIMULATION RESULTS

In this chapter, classification results are presented for the EDAD and MFAB feature extraction algorithms. The two algorithms were executed using a combination of the different databases and classification networks in an effort to produce optimum results. Results are presented in Section A for the EDAB algorithm using the first database and the MLP classification network. Note that the first database consisted of signals only at one carrier frequency. When this algorithm was applied to the second database that contained multiple carrier frequencies, the extension gave poor results. The poor results inspired the development of the MFAB algorithm. This algorithm is capable of processing the more complicated databases (database 2 and database 3). Section B.1 presents results for the MFAB algorithm classified by the MLP using the second database and section B.2 presents results for the MFAB algorithm classified by the MLP with the third database. Section C.1 contains results for the MFAB algorithm classified by the RBF using the second database and section C.2 contains results for the MFAB algorithm classified by the RBF using the third database. Section D contains the results from a SNR study done with the third database.

A. EDAB CLASSIFICATION RESULTS WITH MLP

1. Database 1

The output of the neural network is a confusion matrix which indicates the probability of correct classification. The confusion matrix is commonly used to report results of classification experiments. In a confusion matrix of i rows and j columns the entry in row i, column j records the number of times that an object labeled to be truly of class i was classified as class j. The confusion matrix diagonal, where $i=j$, indicates the successes [27]. Included are the testing results shown for both the Wigner-Ville modulation tests and the signal plus noise tests. Figure 32 shows the classification results for *cdf* threshold, $C = 0.8$ and Figure 33 shows the results for $C = 0.9$. The test results show that increasing the *cdf* threshold from 0.8 to 0.9 within the adaptive binarization algorithm gave poorer classification results in all cases except the BPSK signal.

The following is a list describing the settings of the MLP used to generate the results in Figure 32 and Figure 33:

- 5000 epochs
- Error Goal of 50e-6
- N_1 = 30 neurons first layer
- N_2 = 30 neurons second layer
- N_o = 5 neurons output layer

Test Modulation CM	BPSK	FMCW	FRANK	P4	PT1
BPSK	**0.65**	0.00	0.03	0.00	0.00
FMCW	0.23	**1.00**	0.00	0.00	0.00
FRANK	0.08	0.00	**0.98**	0.03	0.20
P4	0.05	0.00	0.00	**0.98**	0.00
PT1	0.00	0.00	0.00	0.00	**0.80**
Test Noise CM	BPSK	FMCW	FRANK	P4	PT1
BPSK	**0.88**	0.00	0.08	0.02	0.01
FMCW	0.03	**1.00**	0.01	0.04	0.00
FRANK	0.03	0.00	**0.81**	0.07	0.01
P4	0.05	0.00	0.00	**0.87**	0.00
PT1	0.01	0.00	0.10	0.00	**0.98**

Figure 32. Classification Results Showing *C* = 0.8 (Database 1).

Test Modulation CM	BPSK	FMCW	FRANK	P4	PT1
BPSK	**0.73**	0.10	0.03	0.13	0.05
FMCW	0.18	**0.90**	0.03	0.13	0.10
FRANK	0.06	0.00	**0.73**	0.00	0.00
P4	0.04	0.00	0.23	**0.75**	0.15
PT1	0.00	0.00	0.00	0.00	**0.70**
Test Noise CM	BPSK	FMCW	FRANK	P4	PT1
BPSK	**0.71**	0.11	0.07	0.04	0.03
FMCW	0.18	**0.84**	0.09	0.11	0.06
FRANK	0.05	0.02	**0.75**	0.11	0.32
P4	0.06	0.03	0.07	**0.73**	0.08
PT1	0.00	0.01	0.01	0.01	**0.51**

Figure 33. Classification Results Showing *C* = 0.9 (Database 1).

It is important to note that the first algorithm extracted the modulation energy from LPI signals from a database of signals that consisted of only one carrier frequency and when the algorithm was applied to a database with multiple carrier frequencies the extension gave poor results.

B. MFAB CLASSIFICATION RESULTS WITH MLP

To optimize classification with the MFAB algorithm it was necessary to pick an accurate threshold from the histogram derived from the marginal frequency distribution

in order to find the start and stop frequencies of the modulation energy. In order to do so a loop that cycled through each of the histogram bins was used to determine the bin that gives the best threshold for optimum classification. Once the bin that gave the threshold that produced optimum classification was known the classification results were produced. Note that the bins that produced optimum classification for the second database were the same bins that were used for classification with the third database. The optimum bin is related to the feature extraction algorithm and not to the database of signals. That is why it is acceptable to assume that the bin that produced optimum classification with the second database would also produce optimum classification for the third database. Section B.2 contains the optimization tables that were used to determine the bin that corresponds with the threshold that produced the best classification results.

The following is a list describing the settings of the MLP used to generate the results for the second database:

- 5000 epochs
- Error Goal of 1e-6
- N_1 = 35 neurons in the first layer and N_2 = 35 neurons in the second layer for the Choi-Williams and Wigner-Ville distributions
- N_1 = 20 neurons in the first layer and N_2 = 35 neurons in the second layer for the QMFB distribution
- N_o = 5 neurons output layer

1. Database 2

Optimum classification for the Choi-Williams distribution occurred when bin 16 was used as shown in Figures 34 (testing with modulation variation) and 35 (testing with noise variation). No classification results were obtained using thresholds from histogram bins greater than 72 because the feature extraction algorithm could not isolate the modulation.

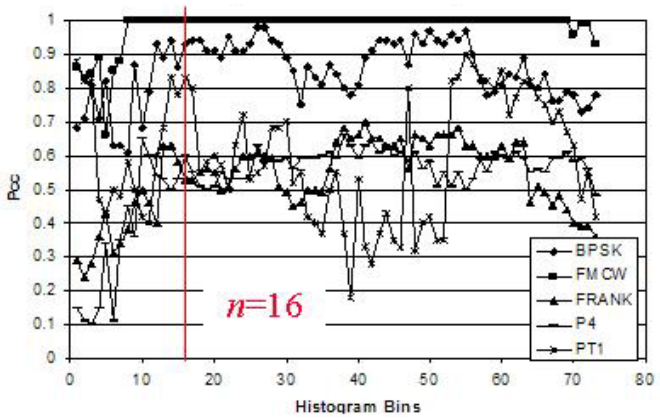

Figure 34. Choi-Williams Optimization Table (Test Modulation).

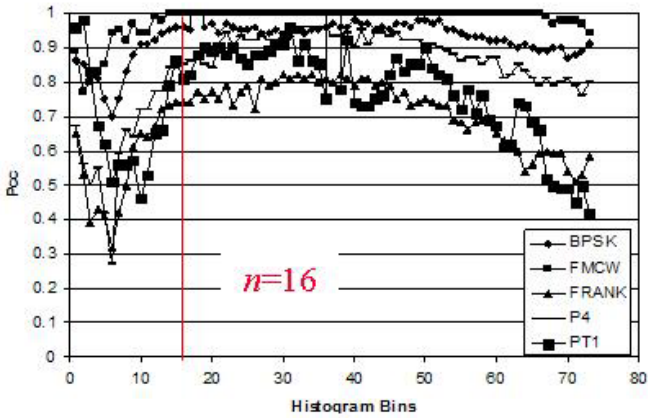

Figure 35. Choi-Williams Optimization Table (Test Noise).

Figure 36 shows the classification results in the form of a confusion matrix for the Choi-Williams distribution. Classifying signals with variations in their modulation is a more difficult case than classifying signals with variations in noise. This trend is present in all of the classification results.

Test Modulation CM	BPSK	FMCW	FRANK	P4	PT1
BPSK	**0.93**	0.00	0.08	0.35	0.08
FMCW	0.00	**1.00**	0.01	0.00	0.00
FRANK	0.01	0.00	**0.53**	0.05	0.07
P4	0.05	0.00	0.35	**0.60**	0.02
PT1	0.01	0.00	0.04	0.00	**0.83**
Test Noise CM	BPSK	FMCW	FRANK	P4	PT1
BPSK	**0.96**	0.00	0.22	0.11	0.12
FMCW	0.00	**1.00**	0.00	0.00	0.00
FRANK	0.01	0.00	**0.74**	0.02	0.03
P4	0.03	0.00	0.01	**0.85**	0.05
PT1	0.00	0.00	0.03	0.01	**0.81**

Figure 36. Choi-Williams Classification Confusion Matrix (*n*=16) (Database 2).

Figure 37 and Figure 38 are the optimization tables for the Wigner-Ville distribution. Optimum classification occurs when bin 31 (n=31) is used. No classification results were obtained using thresholds from histogram bins greater than 66 because the feature extraction algorithm could not isolate the modulation.

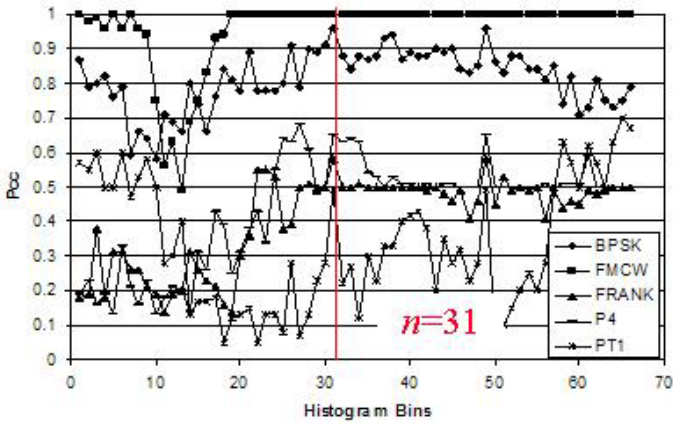

Figure 37. Wigner-Ville Optimization Table (Test Modulation).

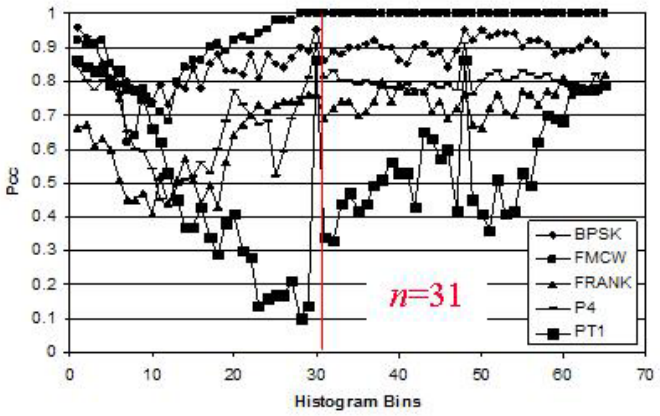

Figure 38. Wigner-Ville Optimization Table (Test Noise).

Figure 39 is the classification results for the Wigner-Ville distribution when bin 31 is used.

Test Modulation CM	BPSK	FMCW	FRANK	P4	PT1
BPSK	**0.96**	0.00	0.08	0.12	0.20
FMCW	0.00	**1.00**	0.00	0.00	0.00
FRANK	0.02	0.00	**0.58**	0.22	0.27
P4	0.02	0.00	0.33	**0.65**	0.04
PT1	0.01	0.00	0.00	0.01	**0.49**
Test Noise CM	BPSK	FMCW	FRANK	P4	PT1
BPSK	**0.95**	0.00	0.19	0.06	0.10
FMCW	0.00	**1.00**	0.00	0.00	0.01
FRANK	0.02	0.00	**0.76**	0.01	0.02
P4	0.01	0.00	0.03	**0.91**	0.01
PT1	0.02	0.00	0.03	0.02	**0.86**

Figure 39. Wigner-Ville Classification Confusion Matrix (*n*=31) (Database 2).

Figure 40 and Figure 41 are the optimization tables for the QMFB distribution. Optimum classification occurs when bin 9 (*n*=9) is used. No classification results were obtained using thresholds from histogram bins greater than 18 because the feature extraction algorithm could not isolate the modulation.

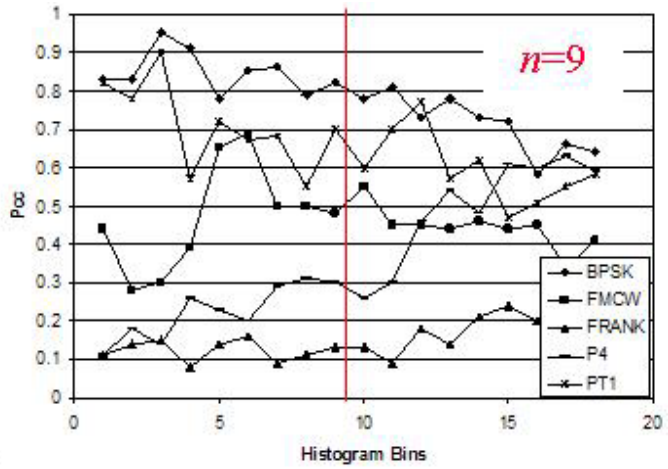

Figure 40. QMFB Optimization Table (Test Modulation).

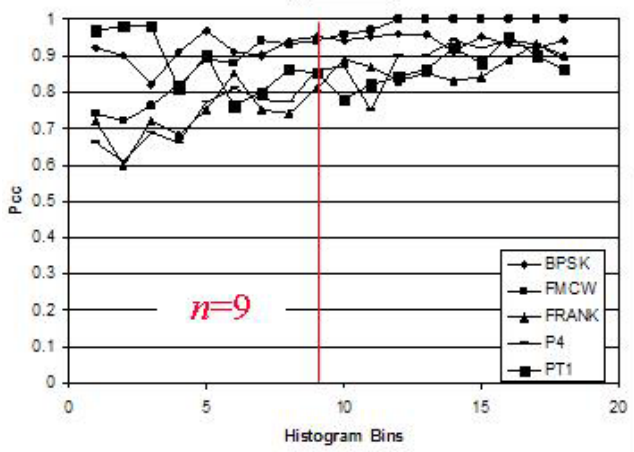

Figure 41. QMFB Optimization Table (Test Noise).

Figure 42 is the classification results for the QMFB distribution when bin 9 is used.

Test Modulation CM	BPSK	FMCW	FRANK	P4	PT1
BPSK	**0.82**	0.40	0.48	0.35	0.23
FMCW	0.14	**0.48**	0.21	0.21	0.00
FRANK	0.01	0.01	**0.13**	0.14	0.05
P4	0.03	0.11	0.18	**0.30**	0.02
PT1	0.00	0.00	0.01	0.00	**0.70**
Test Noise CM	**BPSK**	**FMCW**	**FRANK**	**P4**	**PT1**
BPSK	**0.95**	0.03	0.08	0.11	0.09
FMCW	0.01	**0.94**	0.03	0.01	0.01
FRANK	0.02	0.02	**0.81**	0.01	0.03
P4	0.02	0.02	0.03	**0.86**	0.04
PT1	0.00	0.00	0.05	0.01	**0.85**

Figure 42. QMFB Classification Confusion Matrix (*n*=9) (Database 3).

2. Database 3

In order to improve classification results the MLP was optimized. The MLP was optimized by generating classification results by varying activation functions, the number of neurons in each of the hidden layers, and the performance goal. The following activation functions were tested: logsig, transig, and purelin. For each activation function the number of neurons was varied from, in the first hidden layer, 35 and 45 neurons, and in the second hidden layer, 25, 35, and 45 neurons. Classification results presented for the third database were computed with the optimized MLP. Figure 43 is a plot for the percent correct classification (Pcc) for each of the 15 different configurations of the MLP tested.

Table 6 outlines the specific settings of each of the 15 iterations that were tested for the multi-layer perceptron. Combination 8 was determined to produce optimum results.

Table 6. MLP Optimization Settings

Iteration	Neurons Hidden Layer 1	Neurons Hidden Layer 2	Activation Function 1	Activation Function 2	Activation Function 3	Performance Goal
1	35	25	logsig	logsig	logsig	1.5e-6
2	35	25	tansig	tansig	tansig	2.0e-4
3	35	25	purelin	purelin	purelin	9.0e-2
4	35	35	logsig	logsig	logsig	1.1e-4
5	45	35	logsig	logsig	logsig	1.3e-4
6	45	35	logsig	logsig	purelin	2.0e-4
7	45	35	logsig	logsig	tansig	2.0e-4
8	45	45	logsig	logsig	logsig	1.1e-6
9	55	55	logsig	logsig	logsig	1.1e-6
10	65	65	logsig	logsig	logsig	1.0e-4
11	45	45	logsig	purelin	logsig	8.0e-3
12	45	45	tansig	logsig	logsig	9.8e-7
13	45	45	tansig	tansig	logsig	9.5e-7
14	45	35	tansig	tansig	logsig	9.7e-7
15	45	45	tansig	logsig	tansig	1.0e-4

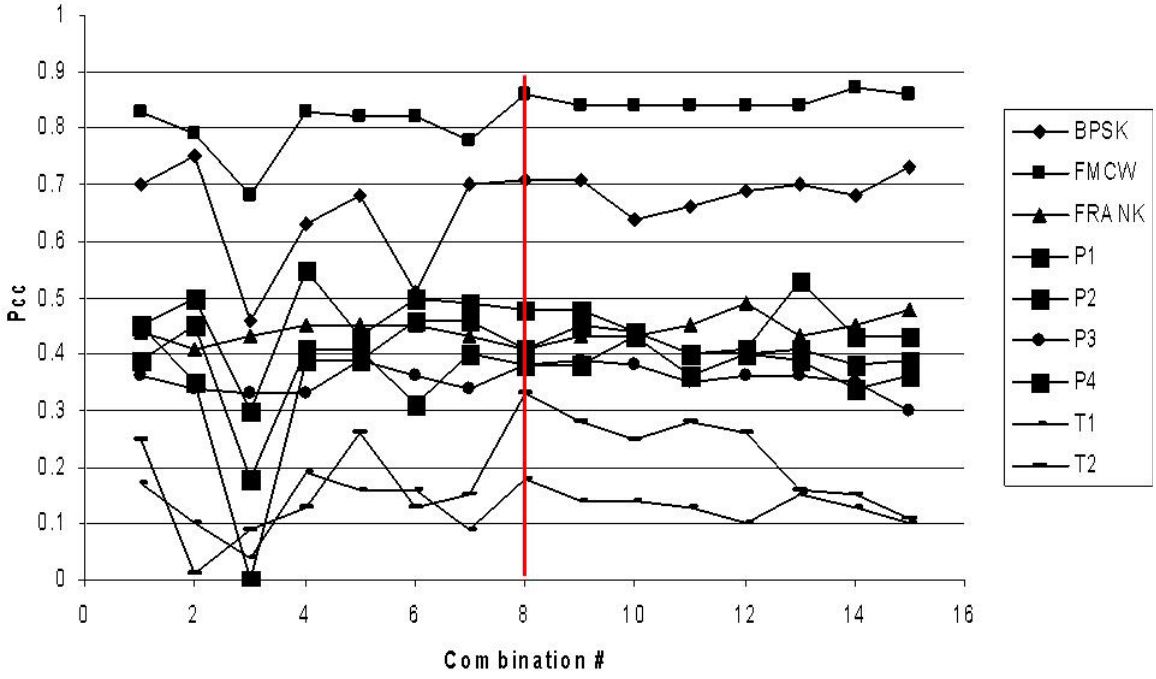

Figure 43. MLP Optimization Table.

The following are the settings that correspond with Combination 8 in Figure 43:

- logsig for each of the three activation functions
- N_1 = 45 neurons in the first hidden layer
- N_2 = 45 neurons in the second hidden layer
- N_o = 5 neurons output layer
- Error goal of 1.1e-6

Figure 44, Figure 45, and Figure 46 are the classification results for the third database with the corresponding optimized bin.

Test Modulation CM	BPSK	FMCW	FRANK	P1	P2	P3	P4	T1	T2
BPSK	**0.71**	0.05	0.05	0.05	0.15	0.10	0.06	0.20	0.20
FMCW	0.04	**0.86**	0.04	0.03	0.08	0.06	0.03	0.19	0.08
FRANK	0.01	0.03	**0.41**	0.20	0.01	0.15	0.19	0.04	0.04
P1	0.05	0.03	0.08	**0.41**	0.16	0.00	0.09	0.15	0.15
P2	0.08	0.02	0.06	0.05	**0.48**	0.09	0.01	0.06	0.01
P3	0.02	0.00	0.16	0.16	0.00	**0.38**	0.19	0.04	0.01
P4	0.04	0.01	0.16	0.09	0.13	0.20	**0.39**	0.09	0.15
T1	0.04	0.00	0.03	0.00	0.00	0.03	0.04	**0.18**	0.04
T2	0.01	0.00	0.01	0.01	0.00	0.00	0.01	0.06	**0.33**

Figure 44. Choi-Williams Classification Confusion Matrix (*n*=16) (Database 3).

Test Modulation CM	BPSK	FMCW	FRANK	P1	P2	P3	P4	T1	T2
BPSK	**0.62**	0.02	0.16	0.08	0.11	0.13	0.11	0.35	0.31
FMCW	0.03	**0.87**	0.08	0.04	0.05	0.09	0.08	0.06	0.05
FRANK	0.07	0.01	**0.39**	0.21	0.14	0.15	0.20	0.06	0.05
P1	0.04	0.01	0.06	**0.33**	0.08	0.08	0.05	0.10	0.10
P2	0.08	0.03	0.08	0.09	**0.51**	0.08	0.05	0.13	0.09
P3	0.03	0.03	0.06	0.13	0.01	**0.34**	0.13	0.04	0.05
P4	0.03	0.03	0.13	0.14	0.04	0.11	**0.38**	0.15	0.21
T1	0.08	0.01	0.00	0.00	0.05	0.03	0.00	**0.06**	0.05
T2	0.03	0.00	0.05	0.00	0.01	0.01	0.01	0.05	**0.09**

Figure 45. Wigner-Ville Classification Confusion Matrix (*n*=31) (Database 3).

Test Modulation CM	BPSK	FMCW	FRANK	P1	P2	P3	P4	T1	T2
BPSK	**0.70**	0.04	0.24	0.10	0.20	0.28	0.10	0.06	0.11
FMCW	0.06	**0.39**	0.29	0.19	0.21	0.20	0.25	0.03	0.00
FRANK	0.01	0.03	**0.11**	0.15	0.08	0.11	0.19	0.06	0.05
P1	0.04	0.06	0.04	**0.16**	0.04	0.09	0.13	0.01	0.04
P2	0.07	0.06	0.08	0.10	**0.10**	0.09	0.14	0.04	0.00
P3	0.02	0.24	0.15	0.16	0.28	**0.15**	0.06	0.01	0.00
P4	0.08	0.18	0.05	0.14	0.09	0.08	**0.13**	0.01	0.23
T1	0.01	0.01	0.03	0.00	0.00	0.00	0.00	**0.65**	0.19
T2	0.01	0.00	0.03	0.00	0.01	0.01	0.01	0.13	**0.39**

Figure 46. QMFB Classification Confusion Matrix (*n*=9) (Database 3).

C. MFAB CLASSIFICATION RESULTS WITH RBF

To produce optimum results with the RBF it was necessary to pick an accurate threshold from the histogram derived from the marginal frequency distribution in order to accurately find the start and stop frequencies of the modulation energy just like was done for the MLP. Section C.2 contains the optimization tables that were used to determine the bin that corresponds with the threshold that produced the best classification results.

1. Database 2

Figure 47 and Figure 48 are the optimization tables for the Choi-Williams distribution. Optimum classification occurs when bin 16 (n=16) is used.

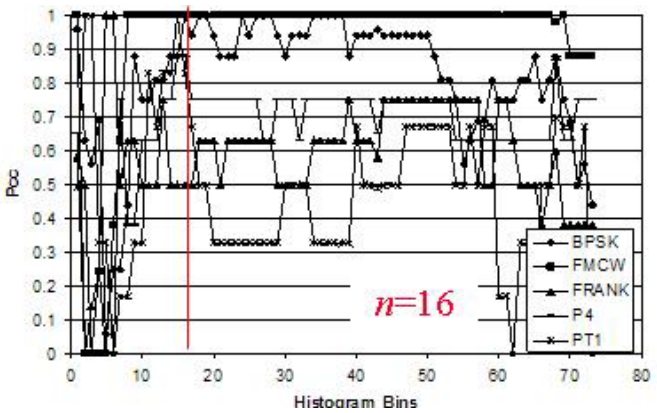

Figure 47. Choi-Williams Optimization Table (Test Modulation).

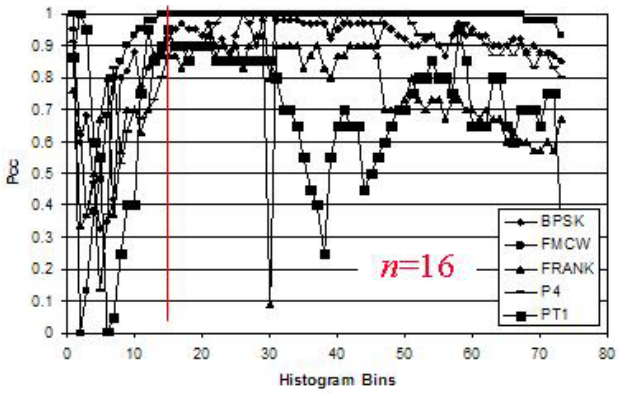

Figure 48. Choi-Williams Optimization Table (Test Noise).

Figure 49 is the classification results for the Choi-Williams distribution when bin 16 is used.

Test Modulation CM	BPSK	FMCW	FRANK	P4	PT1
BPSK	**1.00**	0.00	0.00	0.00	0.17
FMCW	0.00	**1.00**	0.00	0.00	0.00
FRANK	0.00	0.00	**0.50**	0.13	0.00
P4	0.00	0.00	0.38	**0.88**	0.00
PT1	0.00	0.00	0.13	0.00	**0.83**
Test Noise CM	**BPSK**	**FMCW**	**FRANK**	**P4**	**PT1**
BPSK	**0.95**	0.00	0.07	0.07	0.00
FMCW	0.00	**1.00**	0.00	0.00	0.00
FRANK	0.00	0.00	**0.87**	0.00	0.00
P4	0.02	0.00	0.03	**0.90**	0.10
PT1	0.03	0.00	0.03	0.03	**0.90**

Figure 49. Choi-Williams Classification Confusion Matrix (*n*=16) (Database 2).

Figure 50 and Figure 51 are the optimization tables for the Wigner-Ville distribution. Optimum classification occurs when bin 58 (*n*=58) is used.

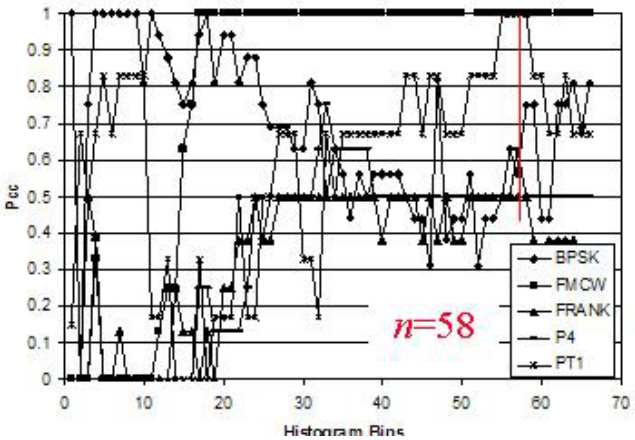

Figure 50. Wigner-Ville Optimization Table (Test Modulation).

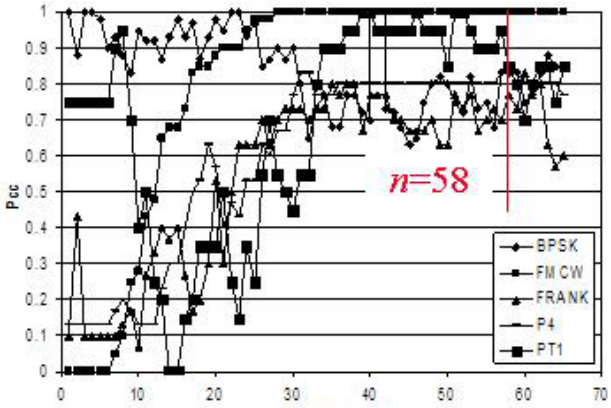

Figure 51. Wigner-Ville Optimization Table (Test Noise).

Figure 52 is the classification results for the Choi-Williams distribution when bin 58 is used.

Test Modulation CM	BPSK	FMCW	FRANK	P4	PT1
BPSK	**0.75**	0.00	0.00	0.00	0.00
FMCW	0.00	**1.00**	0.13	0.00	0.00
FRANK	0.00	0.00	**0.50**	0.38	0.00
P4	0.00	0.00	0.25	**0.50**	0.00
PT1	0.25	0.00	0.13	0.13	**1.00**
Test Noise CM	BPSK	FMCW	FRANK	P4	PT1
BPSK	**0.83**	0.00	0.07	0.03	0.00
FMCW	0.03	**1.00**	0.00	0.00	0.00
FRANK	0.00	0.00	**0.70**	0.10	0.05
P4	0.00	0.00	0.07	**0.83**	0.00
PT1	0.13	0.00	0.17	0.03	**0.95**

Figure 52. Wigner-Ville Classification Confusion Matrix (*n*=58) (Database 2).

Figure 53 and Figure 54 are the optimization tables for the QMFB distribution. Optimum classification occurs when bin 14 (*n*=14) is used.

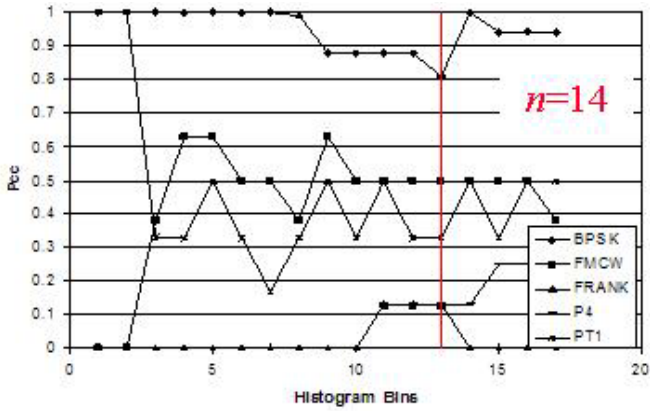

Figure 53. QMFB Optimization Table (Test Modulation).

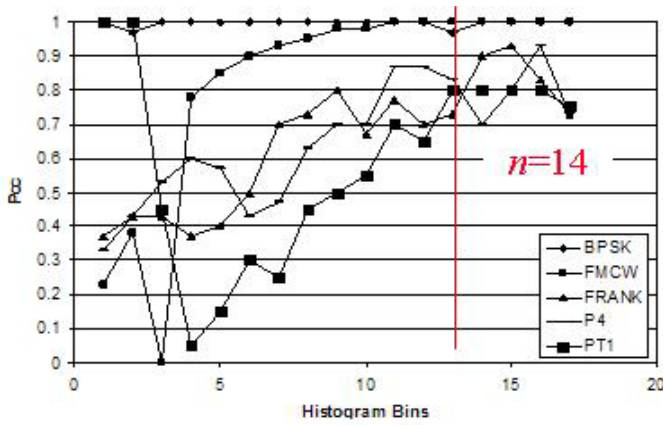

Figure 54. QMFB Optimization Table (Test Noise).

Figure 55 is the classification results for the QMFB distribution when bin 14 is used.

Test Modulation CM	BPSK	FMCW	FRANK	P4	PT1
BPSK	**0.81**	0.25	0.75	0.63	0.67
FMCW	0.19	**0.50**	0.13	0.25	0.00
FRANK	0.00	0.00	**0.13**	0.00	0.00
P4	0.00	0.25	0.00	**0.13**	0.00
PT1	0.00	0.00	0.00	0.00	**0.33**
Test Noise CM	BPSK	FMCW	FRANK	P4	PT1
BPSK	**0.97**	0.00	0.10	0.10	0.20
FMCW	0.03	**1.00**	0.17	0.07	0.00
FRANK	0.00	0.00	**0.73**	0.00	0.00
P4	0.00	0.00	0.00	**0.83**	0.00
PT1	0.00	0.00	0.00	0.00	**0.80**

Figure 55. QMFB Classification Confusion Matrix (*n*=14) (Database 2).

2. Database 3

The RBF was optimized similar to how the MLP was optimized. The RBF was optimized by varying the spread parameter. Each of the three different distributions had a unique spread value that produced optimum classification. Unlike the MLP, each of the different distributions has a unique setting for the RBF to produce optimum results; the MLP had one optimum setting that applied to all three distributions. Figure 56, Figure 57, and Figure 58 are the optimization tables used to determine the best spread value for each of the three different distributions. For the Choi-Williams distribution the optimum spread value was 6, $\sigma = 6$. For the Wigner-Ville distribution the optimum spread value

was 7, $\sigma = 7$. For the QMFB approach the optimum spread value was 2, $\sigma = 2$. Figure 59, Figure 60, and Figure 61 are the results for the optimized RBF.

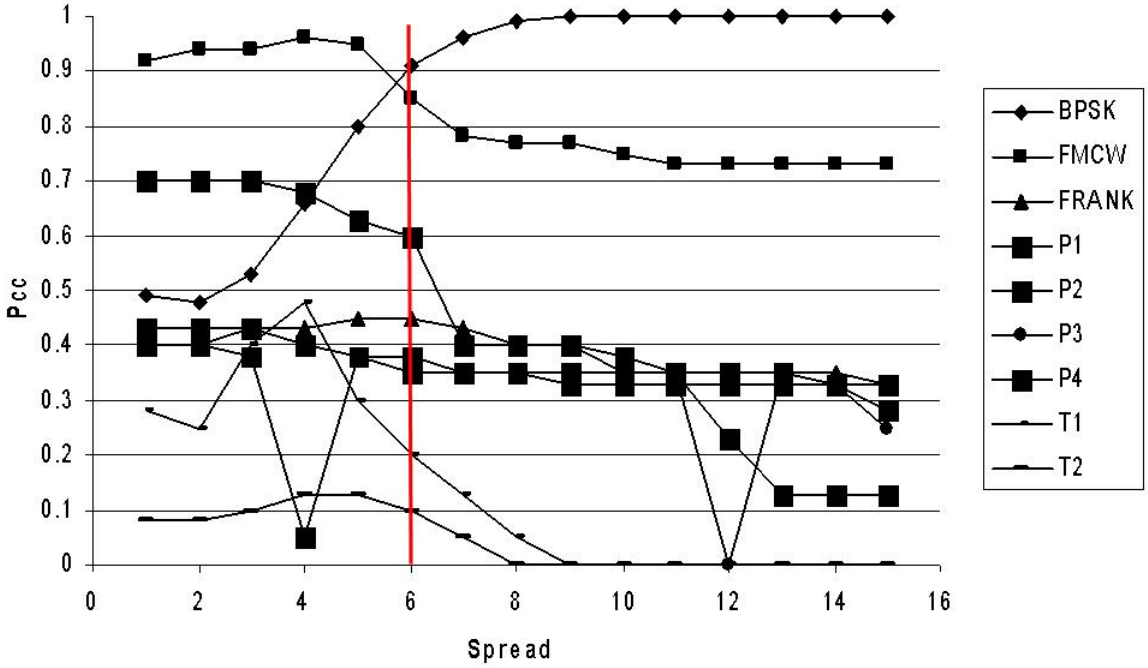

Figure 56. RBF Optimization Table (Choi-Williams).

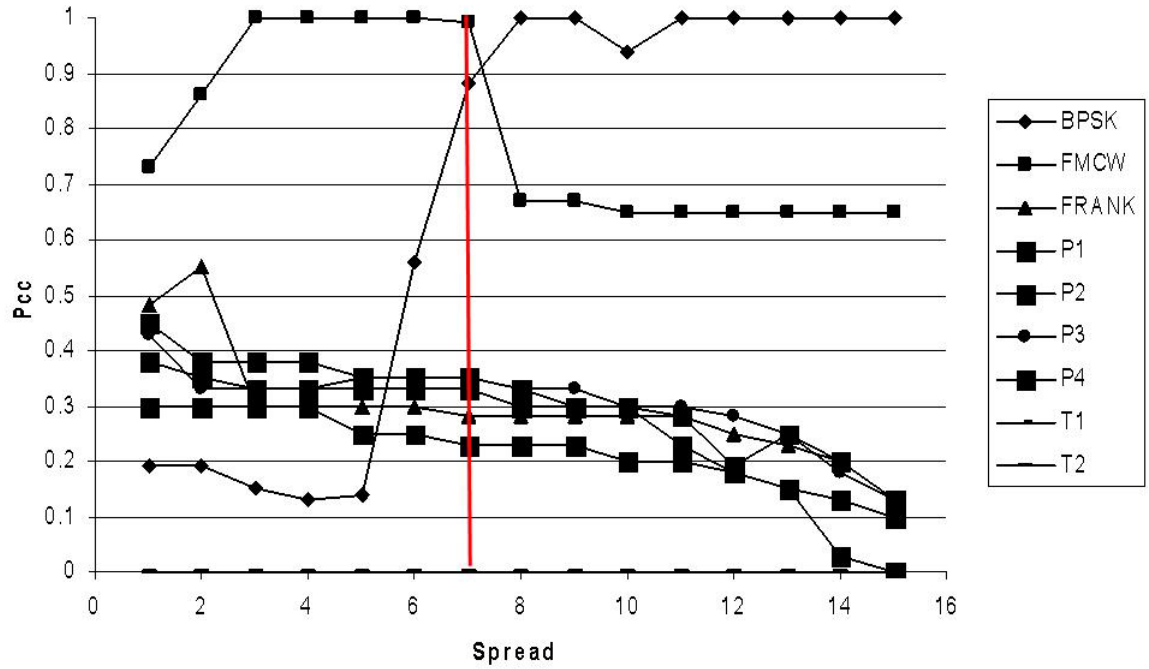

Figure 57. RBF Optimization Table (Wigner-Ville).

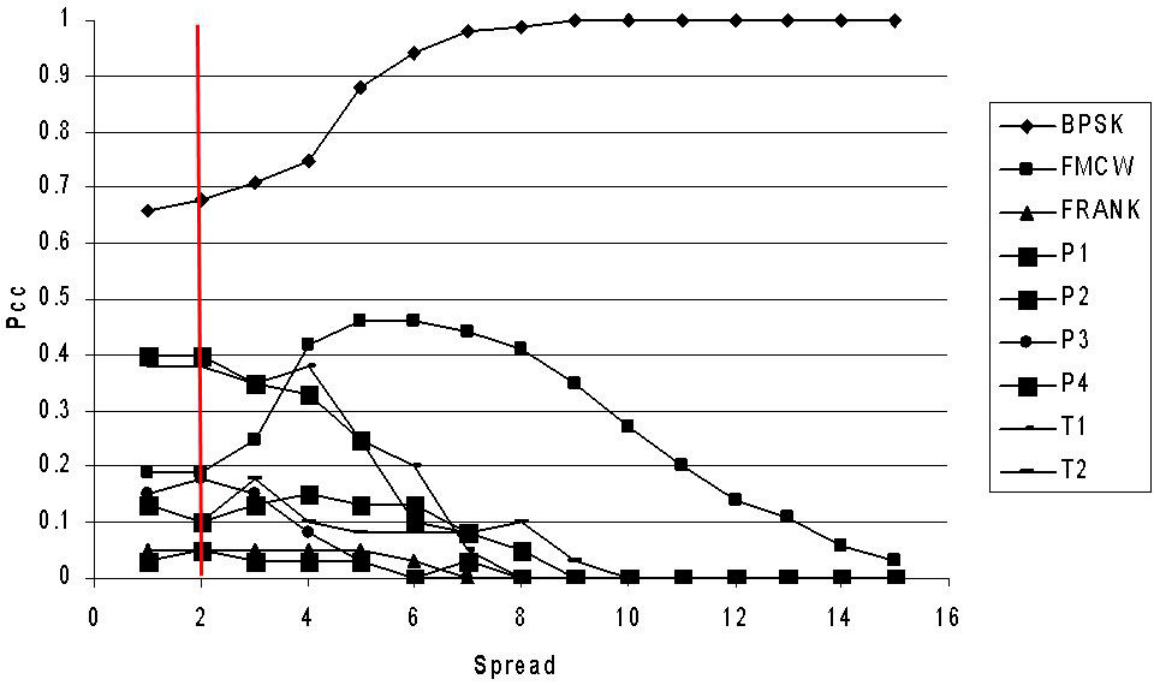

Figure 58. RBF Optimization Table (QMFB).

Test Modulation CM	BPSK	FMCW	FRANK	P1	P2	P3	P4	T1	T2
BPSK	**0.91**	0.15	0.25	0.30	0.25	0.25	0.28	0.75	0.80
FMCW	0.01	**0.85**	0.00	0.00	0.00	0.00	0.00	0.00	0.00
FRANK	0.05	0.00	**0.45**	0.18	0.00	0.18	0.20	0.00	0.00
P1	0.00	0.00	0.00	**0.35**	0.13	0.00	0.00	0.05	0.08
P2	0.00	0.00	0.00	0.00	**0.60**	0.00	0.00	0.00	0.00
P3	0.00	0.00	0.13	0.18	0.00	**0.38**	0.15	0.00	0.00
P4	0.00	0.00	0.15	0.00	0.00	0.18	**0.38**	0.00	0.00
T1	0.03	0.00	0.03	0.00	0.03	0.03	0.00	**0.20**	0.03
T2	0.00	0.00	0.00	0.00	0.00	0.00	0.00	0.00	**0.10**

Figure 59. Choi-Williams Classification Confusion Matrix (σ = 6) (Database 3).

Test Modulation CM	BPSK	FMCW	FRANK	P1	P2	P3	P4	T1	T2
BPSK	**0.88**	0.01	0.25	0.30	0.38	0.25	0.25	0.93	0.95
FMCW	0.13	**0.99**	0.35	0.30	0.28	0.33	0.30	0.08	0.05
FRANK	0.00	0.00	**0.28**	0.08	0.00	0.08	0.10	0.00	0.00
P1	0.00	0.00	0.05	**0.33**	0.00	0.00	0.00	0.00	0.00
P2	0.00	0.00	0.00	0.00	**0.35**	0.00	0.00	0.00	0.00
P3	0.00	0.00	0.00	0.00	0.00	**0.35**	0.13	0.00	0.00
P4	0.00	0.00	0.08	0.00	0.00	0.00	**0.23**	0.00	0.00
T1	0.00	0.00	0.00	0.00	0.00	0.00	0.00	**0.00**	0.00
T2	0.00	0.00	0.00	0.00	0.00	0.00	0.00	0.00	**0.00**

Figure 60. Wigner-Ville Classification Confusion Matrix (σ = 7) (Database 3).

Test Modulation CM	BPSK	FMCW	FRANK	P1	P2	P3	P4	T1	T2
BPSK	**0.68**	0.10	0.40	0.30	0.23	0.38	0.18	0.30	0.38
FMCW	0.08	**0.19**	0.30	0.10	0.35	0.10	0.18	0.00	0.00
FRANK	0.00	0.01	**0.05**	0.03	0.10	0.08	0.03	0.08	0.00
P1	0.04	0.08	0.00	**0.10**	0.03	0.08	0.10	0.05	0.18
P2	0.03	0.08	0.05	0.13	**0.05**	0.03	0.03	0.05	0.03
P3	0.09	0.18	0.08	0.18	0.13	**0.18**	0.10	0.00	0.00
P4	0.10	0.37	0.13	0.18	0.13	0.18	**0.40**	0.05	0.25
T1	0.00	0.00	0.00	0.00	0.00	0.00	0.00	**0.38**	0.08
T2	0.00	0.00	0.00	0.00	0.00	0.00	0.00	0.10	**0.10**

Figure 61. QMFB Classification Confusion Matrix (σ = 2) (Database 3).

D. SNR STUDY

1. Database 3

A study was done with the third database to examine the Pcc versus individual SNRs. Each SNR for a LPI signal is directly related to a range it can be detected by an intercept receiver. The SNR results give an indication of how close in range the emitter must be to achieve a given Pcc. Figure 62, Figure 63, and Figure 64 show how each of the SNRs performed for the three distributions described in this thesis for the variation in modulation. For the Choi-Williams distribution (Figure 62), the best classification results were achieved when a SNR of -1 was used. For the Wigner-Ville distribution (Figure 63), the best classification results were achieved when a SNR of 5 was used. For the QMFB approach (Figure 64), the best classification results were achieved when a SNR of 3 was used.

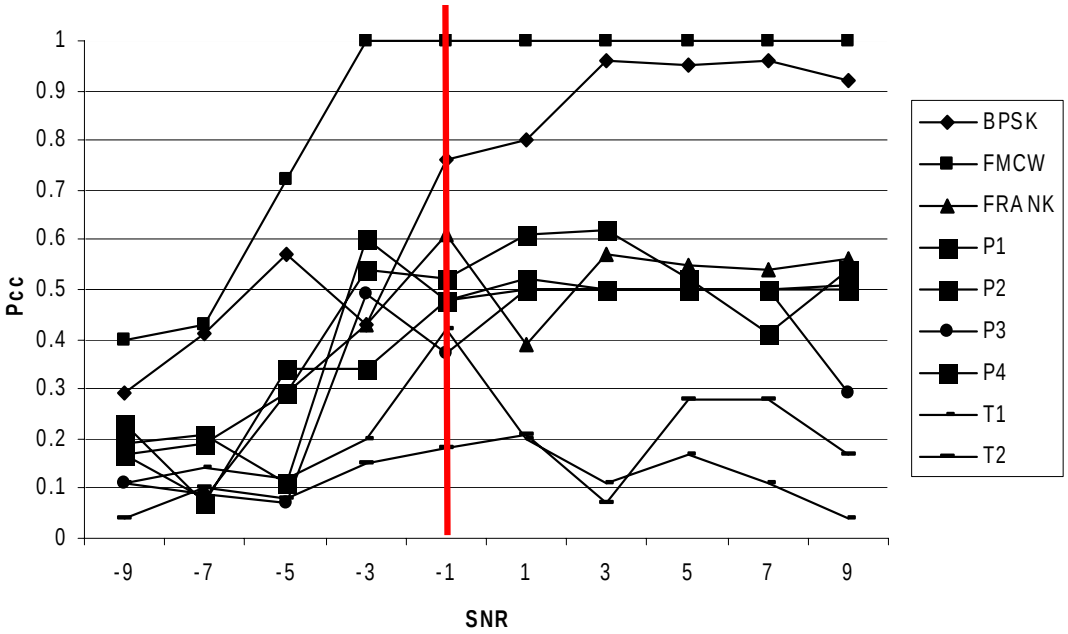

Figure 62. Choi-Williams SNR Study

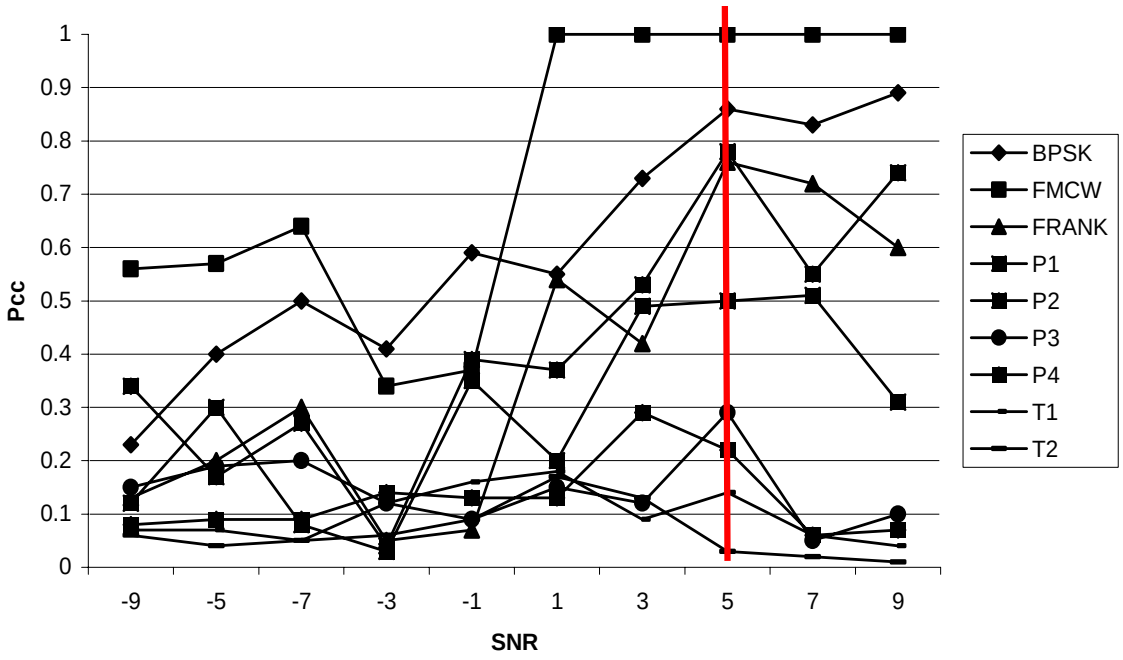

Figure 63. Wigner-Ville SNR Study

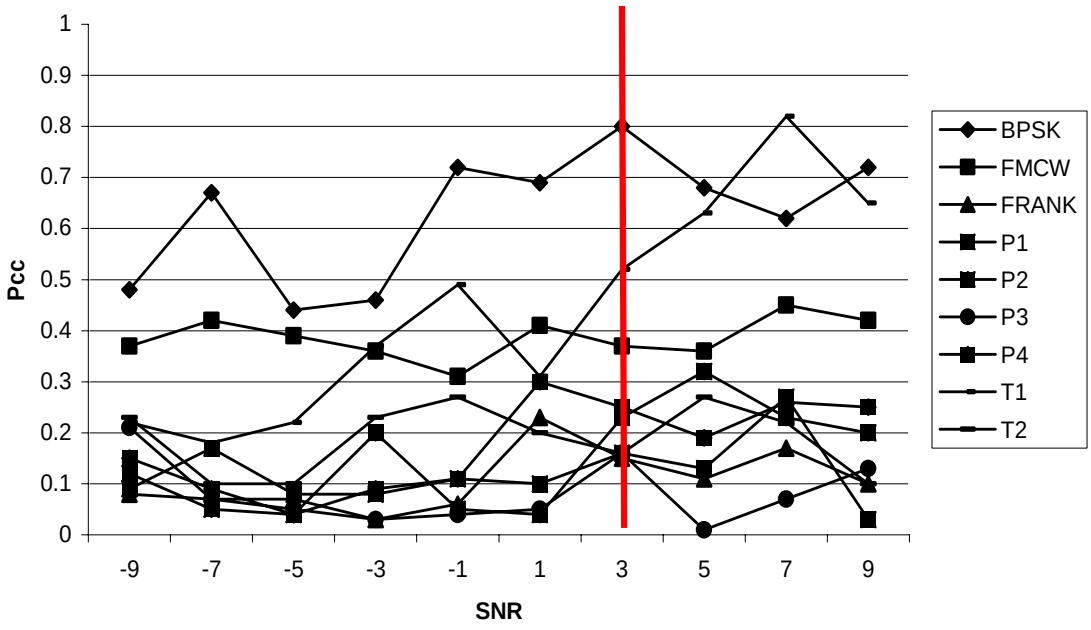

Figure 64. QMFB SNR Study

THIS PAGE INTENTIONALLY LEFT BLANK

VIII. CONCLUSIONS AND RECOMMENDATIONS

A. CONCLUSIONS

1. Feature Extraction Algorithms

The EDAB process was the first algorithm tested. The algorithm proved to be successful only when the algorithm was applied to a database of signals that contained only one carrier frequency. When the algorithm was applied to a database that contained signals at two carrier frequencies it did not perform well. The combination of multiple carrier frequencies in instances with high SNRs confused the algorithm; it could not isolate the modulation's carrier frequency. Morphological operations have a lot of potential in terms of processing LPI signals and can be extended to a more diverse database of LPI signals if the correct combinations of morphological operations are applied.

The MFAB process was the second and most successful algorithm. It was able to be applied to a complex database of LPI signals that closely resembled the types of signals that are found operationally and produce promising results. Part of the MFAB algorithm's success was the user's ability to choose a comparator threshold from an optimization table. Choosing an optimum threshold ensured that the algorithm was able to isolate the modulation energy and produce best possible results.

The Fast Image Filtering algorithm was successful not because it was able to extract the modulation energy from a LPI signal autonomously but because it established itself as a technique that can be implemented with the EDAB and MFAB algorithms to reduce noise in a LPI signal. Minimizing noise in a LPI signal simplifies the feature extraction process.

2. Classification Results

In terms of classification, the best results were produced with the Choi-Williams distribution. The success of the Choi-Williams distribution can be attributed to its lack of cross terms. The Wigner-Ville distribution has large cross-terms which can confuse the classification networks. Large cross-terms are not conducive to producing unique features that can distinguish the different signals from one another.

The MLP consistently produced better results than the RBF. The MLP was successful because it had more variables that could be configured to produce optimum results. The only variable in the RBF that could be changed was the spread. While the results from the RBF were not as good as those seen coming from the MLP the RBF does have an advantage in terms of its application to an operational environment. Its training phase is fast and efficient. Because it trains faster than the MLP, in an operational environment a user would not have to wait long before receiving classification results for a LPI signal. This feature of the RBF is important and should be investigated in an attempt to improve the RBF's results so that one day it can be applied operationally.

3. Applicability to Defense Applications

To counter the threat posed by LPI radars it is necessary to develop an autonomous sequence that can autonomously detect, extract features, and classify LPI signals. Automating this sequence and emitting any human-in-the-loop participation allows for war fighters operating globally to receive real-time intelligence. The conflicts that currently burden our country require that all war fighters receive intelligence promptly. Automating the LPI classification process brings the war fighter one more piece of real-time intelligence that can help him safely and expeditiously accomplish his mission.

B. RECOMMENDATION FOR FUTURE WORK

All of the feature extraction algorithms can be further investigated to improve performance. The EDAB algorithm introduced the idea of combining unique morphological operations to extract the modulation energy from LPI signals. The EDAB algorithm can be applied to more complex databases of LPI signals if the correct combinations of morphological operations are used. The MFAB algorithm was able to be applied to a complex database of LPI signals and produce promising results. However, the results were not perfect and improving the algorithm to increase results needs to be examined. Implementing the Fast Image Filtering technique with the EDAB and MFAB algorithms as a step to eliminate noise in LPI signals needs to be investigated.

The classification networks were optimized in this thesis in an attempt to improve results. However, the optimization process can be improved in order to improve results.

Different aspects of the networks can be examined in an attempt to continue the optimization process.

The ultimate goal that motivates research in the field of autonomous T-F cropping and feature-extraction algorithms for classification of LPI radar modulations is applying the technology on to a high-speed processor that can be embedded in a ELINT receiver that supports theatre operations globally.

THIS PAGE INTENTIONALLY LEFT BLANK

LIST OF REFERENCES

[1] Pace, P.E., *Detecting and Classifying Low Probability of Intercept Radar*, Boston: Artech House, 2004.

[2] Perrson, C., "Classification and Analysis of Low Probability of Intercept Radar Signals Using Image Processing," Master's Thesis, Naval Postgraduate School, Monterey, California, 2003.

[3] Schleher, D.C. "Low Probability of Intercept Radar," IEEE International Radar Conference, pp. 346-349, 1985.

[4] GuoSui, L, Hong, G, WeiMin, S, HongBo, S., "The Analysis and Design of Modern Low Probability of Intercept Radar," International Conference on Radars, pp. 120-124, October 2001.

[5] Parker, J.R., *Algorithms for Image Processing and Computer Vision*, New York: Wiley Computer Publishing, 1997.

[6] Person, C., Yeo, S-Y, Zilberman, E.R., Pace, P.E., "Autonomous Classification of LPI Radar CW Modulations," IEEE (in review), January 2006.

[7] Piper, S. O., "Homodyne FMCW radar range resolution effects with sinusoidal nonlinearities in the frequency sweep," Record of the IEEE International Radar Conference, pp. 563--567, 1995.

[8] Frank, R. L., "Polyphase codes with good nonperiodic correlation properties," IEEE Trans. IT-9, pp. 43 – 45, 1963.

[9] Lewis, B.L. "Range-time-sidelobes reduction technique for FM-derived polyphase PC codes," IEEE Trans. on Aerospace and Electronic Systems, Vol. 20, No. 3., pp. 834-840, July 1993.

[10] Lewis, B.L., Kretschmer, F.F., and Shelton, W.W., *Aspects of Radar Signal Processing*, Artech House Inc., Norwood, MA, 1986.

[11] Fielding, J.E., "Polytime Coding as a Means of Pulse Compression," *IEEE Trans. On Aerospace and Electronic Systems*, Vol. 35, No. 2, pp. 716-721, 1999.

[12] Barker, R.H., "Group synchronizing of binary digital systems in communication theory," Butterworth, London, pp. 273-287, 1953.

[13] Gau, J.Y., "Analysis of LPI Radar Signals Using Wigner Distribution," Master's Thesis, Naval Postgraduate School, Monterey, California, 2002.

[14] Haykin, S., Bhattacharya, T., “Wigner-Ville Distribution: An Important Functional Block for Radar Target Detection in Clutter,” Conference record of the 28th Asilomar on Systems and Computers, Vol. 1, pp. 68-72, 1994.

[15] Cohen, L., “Time-frequency distributions-A review,” Proceedings of the IEEE, Vol. 77, p 950, 1989.

[16] Zilberman, E.R., Pace, P.E., “Autonomous Time-Frequency Feature Extraction Algorithm for LPI Radar Modulation Classification,” Proceedings of the IEEE International Conference on Image Processing, October 8-11, 2006.

[17] Zilberman, E.R., Pace, P.E., “Autonomous Cropping and Feature Extraction Using Time-Frequency Marginal Distributions for LPI Radar Classification,” Proceedings of the Eighth IASTED International Conference on Signal and Image Processing, August 14-16, 2006.

[18] Gonzalez, R. C., Woods, R.E., and Eddins, S.L., *Digital Image Processing Using MATLAB.* New Jersey: Prentice Hall, 2004.

[19] Maragos, P., “Differential morphology and image processing,” IEEE Transactions on Image Processing, Vol. 5, No. 6, pp. 922 – 937, June 1996.

[20] Chen, S., and Haralick, R.L., **“**Recursive erosion, dilation, opening, and closing transforms,” IEEE Transactions on Image Processing, Vol. 4, No. 3, pp. 335 – 345, March 1995.

[21] Van De Ville, D., Van de Walle, R., Philips, W., and Lemahieu, I., “Image resampling between orthogonal and hexagonal lattices,” Proc. 2002 International Conference on Image Processing, Vol. 3, pp. III-389 - III-392, 24-28 June 2002.

[22] Krishnan, S., “Instantaneous mean frequency estimating using adaptive time-frequency distributions,” Canadian Conference on Electrical and Computer Engineering, Vol. 1, pp 141-146, May 2001.

[23] Uzan, I.S., Bouridane, A.A., “FPGA Implementation of Fast Fourier Transforms for Real-Time Signal and Image Processing,” IEEE Conference on Field-Programmable Technology (FPT), pp. 102-109, 2003.

[24] Narayan, S., Tagliarini, G.A., and Page, E., “Enhancing MLP Networks using a Distributed Data Representation,” IEEE Transactions on Systems, Man, and Cybernetics, Vol. 26, pp. 143-149, 1996.

[25] Wong, T., Lo, T., Leung, H., Litva, J., Bosse, E., “Low-Angle Radar Tracking Using Radial Basis Function Neural Network,” IEE Proceedings for Radar and Signal Processing, Vol. 140, pp. 323-328, 1993.

[26] Theodoridis, S., and Koutroumbas, K., *Pattern Recognition*, San Diego: Academic Press, 1999.

[27] Shapiro, L.G., Stockman, G.C., *Computer Vision*, New Jersey: Prentice Hall, 2001.

THIS PAGE INTENTIONALLY LEFT BLANK

INITIAL DISTRIBUTION LIST

1. Defense Technical Information Center
   Ft. Belvoir, VA

2. Dudley Knox Library
   Naval Postgraduate School
   Monterey, CA

3. Professor Dan Boger
   Naval Postgraduate School
   Monterey, CA

4. Professor Don Brutzman
   Naval Postgraduate School
   Monterey, CA

5. Professor Phillip Pace
   Naval Postgraduate School
   Monterey, CA

6. Mr. Al DiMatlesa
   NRL Code 5701
   Washington D.C.

7. Mr. Bob Kusuda
   ONR Code 313
   Arlington, VA

8. Mr. Bruce Moses
   L-3 Communications
   New York, NY

9. ENS Eric R. Zilberman
   United States Navy
   Belmont, CA

10. Dr. Frank Klemm
    NRL Code 5700
    Washington D.C.

11. Mr. Jim Durbin
    ONR Code 313
    Arlington, VA

12. Mr. Jim Talley
ONR Code 313
Arlington, VA

13. Mr. Joe McGovern
ONI
Washington D.C.

14. Mr. Mike Monsma
ONR Code 313
Arlington, VA

15. Mr. Mike Mucachio
ONI
Washington D.C.

16. Dr. Peter Craig
ONR Code 313
Arlington, VA

17. Dr. Scott Baker
L-3 Communications
New York, NY

18. Dr. Ted Roberts
NRL Code 5700
Washington D.C.